

REPORT DOCUMENTATION PAGE

OMB No. 0704-0188

Public reporting burden for this collection of information is estimated to average 1 hour per response, including the time for reviewing instructions, searching data sources, gathering and maintaining the data needed, and completing and reviewing the collection of information. Send comments regarding this burden estimate or any other aspect of this collection of information, including suggestions for reducing this burden to Washington Headquarters Service, Directorate for Information Operations and Reports, 1215 Jefferson Davis Highway, Suite 1204, Arlington, VA 22202-4302, and to the Office of Management and Budget, Paperwork Reduction Project (0704-0188) Washington, DC 20503.

PLEASE DO NOT RETURN YOUR FORM TO THE ABOVE ADDRESS.

1. REPORT DATE (DD-MM-YYYY) 1 January 2004	2. REPORT TYPE Final Technical Report	3. DATES COVERED (From – To) 1 January 2004 – 31 December 2006
4. TITLE AND SUBTITLE CFD Code Validation Experiments for Hypersonic High-Enthalpy Flows		5a. CONTRACT NUMBER
		5b. GRANT NUMBER FA9550-04-1-0114
		5c. PROGRAM ELEMENT NUMBER
6. AUTHOR(S) Dr. Graham V. Candler		5d. PROJECT NUMBER
		5e. TASK NUMBER
		5f. WORK UNIT NUMBER
7. PERFORMING ORGANIZATION NAME(S) AND ADDRESS(ES) Department of Aerospace Engineering and Mechanics University of Minnesota Minneapolis MN 55455		8. PERFORMING ORGANIZATION REPORT NUMBER
9. SPONSORING/MONITORING AGENCY NAME(S) AND ADDRESS(ES) USAF/AFRL AFOSR/N/A 875 North Randolph Street Arlington VA 22203 <i>Dr. John Schnusseur</i>		10. SPONSOR/MONITOR'S ACRONYM(S) AFOSR
		11. SPONSORING/MONITORING AGENCY REPORT NUMBER N/A

12. DISTRIBUTION AVAILABILITY STATEMENT

Distribution Statement A: Approved for public release, distribution unlimited

AFRL-SR-AR-TR-07-0242

13. SUPPLEMENTARY NOTES

14. ABSTRACT

During the past three years, we have worked to develop and analyze a high-enthalpy flow dataset for CFD code validation. In collaboration with CUBRC Inc. personnel, we designed the experimental conditions for the double-cone geometry used in previous low-enthalpy nitrogen tests. We then used our standard CFD codes and thermo-chemical models to analyze these flows. In general, the comparisons with nitrogen flows are good, even at high enthalpy (10MJ/kg). But the comparisons between predictions and experiments for air above 5MJ/kg is poor. We find that as the enthalpy increases, the agreement gets worse. In particular, the CFD predicts that the separation zone decreases in size much more rapidly than given in the experiments.

15. SUBJECT TERMS

16. SECURITY CLASSIFICATION OF:			17. LIMITATION OF ABSTRACT Unclassified	18. NUMBER OF PAGES 68	19a. NAME OF RESPONSIBLE PERSON
a. REPORT Unclassified	b. ABSTRACT Unclassified	c. THIS PAGE Unclassified			19b. TELEPHONE NUMBER (Include area code) (703)
					Standard Form 298 (Rev. 8-98) Prescribed by ANSI-Std Z39-18

FINAL TECHNICAL REPORT

Period: 01 Jan 04 - 31 Dec 06

CODE VALIDATION STUDIES OF HIGH-ENTHALPY FLOWS

AIR FORCE OFFICE OF SCIENTIFIC RESEARCH

Grant No. FA9550-04-1-0114

Graham V. Candler

Ioannis Nompelis

Department of Aerospace Engineering and Mechanics

University of Minnesota, Minneapolis MN 55455

candler@aem.umn.edu

612-625-2364 Fax: 612-626-1558

Summary

There is growing interest in validating existing numerical methods and physical models employed in currently state-of-the-art computational fluid dynamics (CFD) codes. The numerical methods and physical models that are under examination and are the subject of validation studies pertain to the simulation of hypersonic low Reynolds number flows that are in the continuum and the near continuum limit. This work was based on the framework that we established for the validation of numerical methods for inert hypersonic flows under Air Force support in recent years.

In the past, we simulated experiments of hypersonic laminar double-cone flows that were performed at the Large Energy National Shock (LENS) facility. The experiments were conducted as part of a validation effort for continuum and particle-based codes. The double-cone flow was chosen because it exhibits strong viscous/inviscid and shock interactions, and we have shown that the separation zone that forms at the cone-cone juncture is sensitive to both the amount of numerical dissipation in the numerical scheme and the amount of energy that participates in the dissociation process and other chemical relaxation phenomena (real-gas effects). The double-cone flows are very challenging to compute even with present day computing power. As a result of the previous effort, a large number of experiments were performed in air under high enthalpy conditions. The experiments were performed in different facilities at LENS, and data exists for a range of free-stream Mach and Reynolds numbers at various level of free-stream enthalpy. Simulations of these experiments that employ standard chemical kinetics models showed poor agreement with the experimental data. Agreement worsens as the free-stream enthalpy is increased. Most of present work focuses on the analysis of the experimental conditions. Effort was put forth to analyze these high enthalpy experiments by employing the most up-to-date physical models of high enthalpy air chemistry.

In particular, we used a vibrational state-specific model for vibrational relaxation in the LENS nozzle flow. We also considered a wide variety of thermo-chemical models and chemical kinetics models for rapid expansion of air in a hypersonic nozzle. To date, these modeling approaches have been unsuccessful for high enthalpy air. We find that once the equilibrium composition of the reservoir gas has an appreciable level of oxygen atoms, we obtain poor agreement with measurements in the LENS facility. This occurs above about 5 MJ/kg in air. We are continuing to work on this problem, and this report documents what we have tried to date.

I. Introduction

1. Motivations

There has been a great deal of interest in developing prototype re-entry vehicles and hypersonic air-breathing vehicles for access to space. These vehicles will be designed to operate in the high enthalpy regime, where the flow exhibits high enthalpy or “real-gas” effects. Real-gas effects are triggered by the high temperatures encountered in high enthalpy flows. These effects include excitation of the internal energy modes of the gas, as well as dissociation of polyatomic species and ionization. These physical phenomena occur over a range of time scales, and the flow is frequently in chemical and thermal nonequilibrium. Additionally, depending on the shape of the vehicle and the flight conditions, shock/shock interactions and viscous-inviscid interactions will likely occur during flight at hypersonic speeds. The combined effects of these phenomena and real-gas chemistry may dramatically alter the flight characteristics of the vehicle. Therefore, all of these effects must be taken into consideration in the development stage of future hypersonic vehicles.

The development and design of such vehicles is aided by the use of experimentation and numerical simulation. There are difficulties associated with both approaches. It is difficult to produce ground-based hypersonic flow experiments that are realistic in terms of the enthalpy and composition of the gas. It is also difficult to perform accurate numerical simulations, as the physics involved is not fully understood.

2. Double-Cone Flows

Flows generated by double-cone geometries placed in hypersonic free-streams have been studied in the past. Earlier studies of these flows focused primarily on testing and improving nonequilibrium chemistry models. This is because the double-cone flows are sensitive to high enthalpy effects. These studies were largely unsuccessful. In more recent work, we studied double-cone flows for the purpose of validating numerical methods. This was the first step in a “building-block” approach to assess the ability of computational fluid dynamics codes to reproduce complex hypersonic flows from the low enthalpy to the high enthalpy regime. The effort was proven successful in terms of validating the numerical methods by making comparisons with experimental measurements of double-cone flows in inert environments at low enthalpy conditions.

The flow generated by a double-cone configuration placed in a hypersonic free-stream, exhibits strong viscous-inviscid and shock/shock interactions. The oblique shock generated by the first, shallow-angle cone, interacts with the shock generated by the second cone. When the second cone angle is larger than a critical angle, this shock is detached, and the interaction is very strong. A schematic of the flow generated by a double-cone in a nitrogen

free-stream at a Mach number of about 12 is shown in Fig. 1. In this figure, the model has a first cone half-angle of 25° and a second cone half-angle of 55° . The shock structure and subsonic regions are outlined, and the shear layers are visualized. The oblique shock interacts with the bow shock generated by the second cone, and a transmitted shock is formed, which impinges on the surface downstream of the cone-cone juncture. The adverse pressure gradient at the cone-cone juncture causes the boundary layer to separate. The separated region that forms at the corner creates its own shock, which interacts with the bow shock. This shifts the point of interaction, which in turn alters the separation zone. This process feeds back on itself until the flow reaches steady state – if a steady state exists. A supersonic jet is formed along the surface of the second cone downstream of the impingement point, and it undergoes a series of isentropic compressions and expansions. The flow behind the strong bow shock is subsonic, and therefore the shape of the jet influences the shock structure.

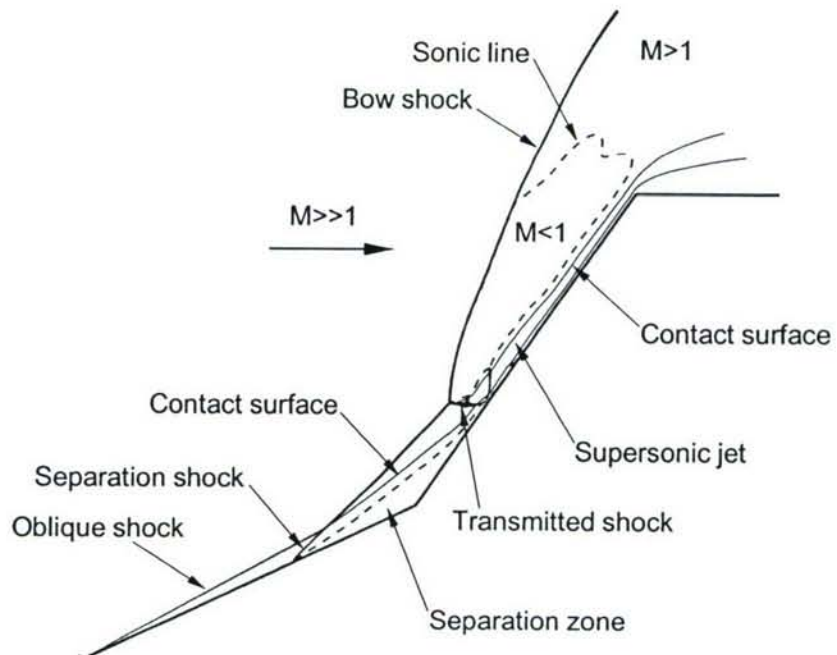


Figure 1. Schematic diagram of a typical flow-field generated by a 25° - 55° double-cone geometry placed in a Mach 12 free-stream. The flow is from left to right, and a slice is shown of flow that is circularly symmetric about the axis of the geometry.

Under high enthalpy conditions, the chemical processes that take place in the flow are tightly coupled with the fluid motion through energy exchange mechanisms. In high enthalpy double-cone flows, dissociation takes place both in the high temperature region behind the bow shock, and inside the separation zone. In these regions, the highly energetic particles undergo collisions and lose some of their energy by causing dissociation of polyatomic species. By this process, energy is removed from the bulk flow and stored in the form of chemical energy. The rate at which this process takes place greatly impacts the mean flow. Thus, the size of the embedded region of separation is sensitive to chemical effects in the flow. Additionally, the size of the separation zone may be measured experimentally by surface measurements such as surface pressure and heat transfer rate. Thus, we can make direct comparisons between numerical predictions and experimental measurements.

3. Summary of Previous Work

We have studied extensively hypersonic double-cone flows with and in the absence of flowfield chemistry. In earlier work related to CFD code validation, we analyzed experiments performed at the Large Energy National Shock (LENS) facility. We studied low enthalpy laminar double-cone flows and showed that because these experiments were performed at low pressure, there was vibrational energy frozen in the free-stream, which in turn reduced the amount of kinetic energy that was used to infer the free-stream conditions via a Pitot pressure measurement. This resulted in erroneously inferring the free-stream conditions, which resulted in seeing discrepancies between the experimental measurements and the numerical predictions. When we accounted for that effect in numerical simulations, and also augmented the boundary conditions formulation to account for the slip effects due to the low pressures of the experiment, we observed excellent agreement between calculations and experiments for a number of cases. Fig. 2 plots the computed and measured heat transfer rates to the double-cone model for low enthalpy nitrogen flows at Mach 9 (Run 28) and Mach 12 (Run 35). These calculations were performed at the newly inferred free-stream conditions and with the slip model for the internal energy modes at the wall. Fig. 3 plots the computed and measured heat transfer rates to the double-cone model for low enthalpy Mach 15 nitrogen flows at very low pressures. Run 4 is referred to as “1/2 density case” and Run 5 as “1/3 density case” and these designations are with reference to Run 35. These two experimental conditions were designed to provide a test-case for the more computationally intensive DSMC methods. Agreement is excellent between the CFD predictions and the experimental measurements for these cases.

We observed good agreement for flows of nitrogen at moderate enthalpy conditions (free-stream specific enthalpy of 5 MJ/kg), and the results are plotted in Fig. 4, which plots the predicted heat transfer to the wall along with experimental data for Mach 10

flow. The result obtained under the computed conditions is very similar to the original predicted result. The computed conditions were obtained by performing calculations of the nozzle flow with CFD at the conditions of the experiment. The computed conditions were extracted from the CFD simulation at the location where the model is situated.

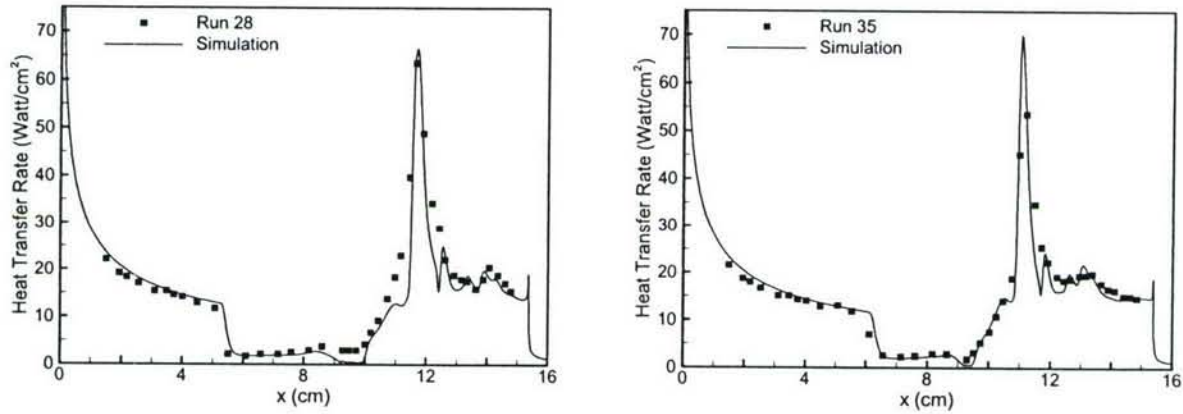


Figure 2. Computed heat transfer rate for low enthalpy nitrogen at Mach 9 (Run 28) and Mach 12 (Run 35).

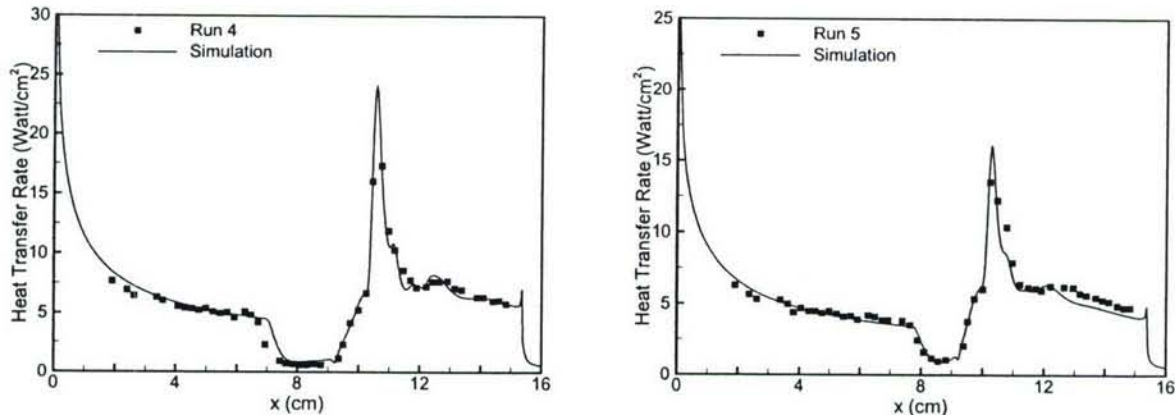


Figure 3. Computed heat transfer rate to the wall for the nominally Mach 15 nitrogen flows Run 4 (“1/2 density case”) and Run 5 (“1/3 density case”).

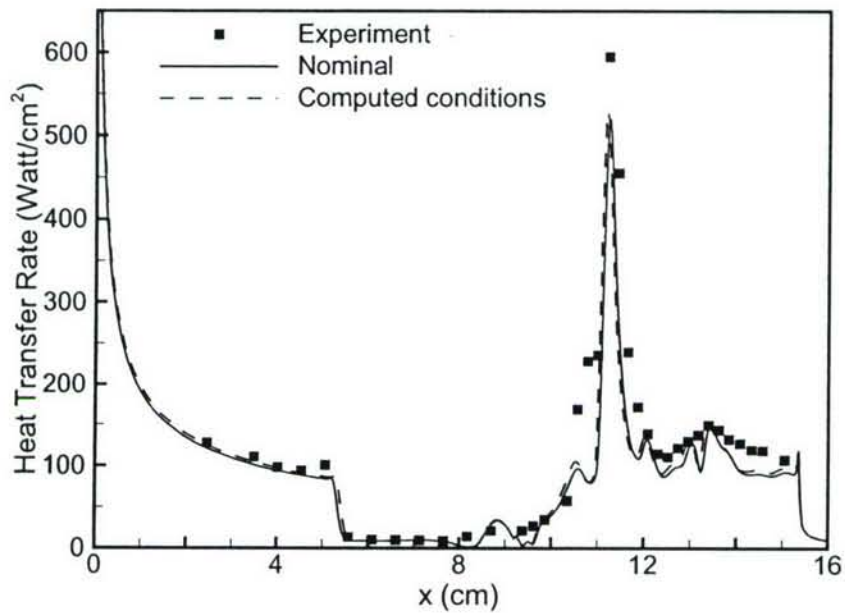


Figure 4. Computed heat transfer rate to the wall for Mach 10 nitrogen flow at moderate enthalpy conditions (Run 42).

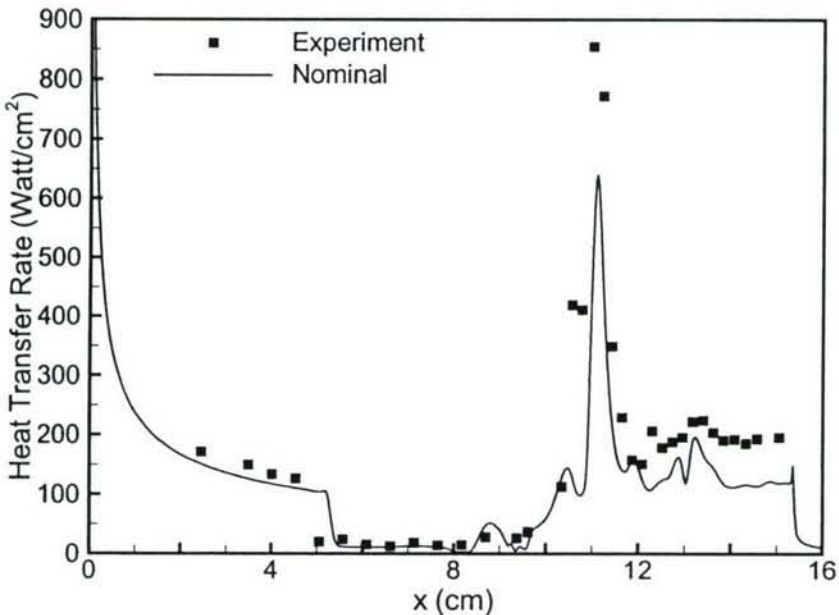


Figure 5. Computed heat transfer rate to the wall for Mach 10 nitrogen flow at moderate enthalpy conditions and higher free-stream Reynolds number (Run 46).

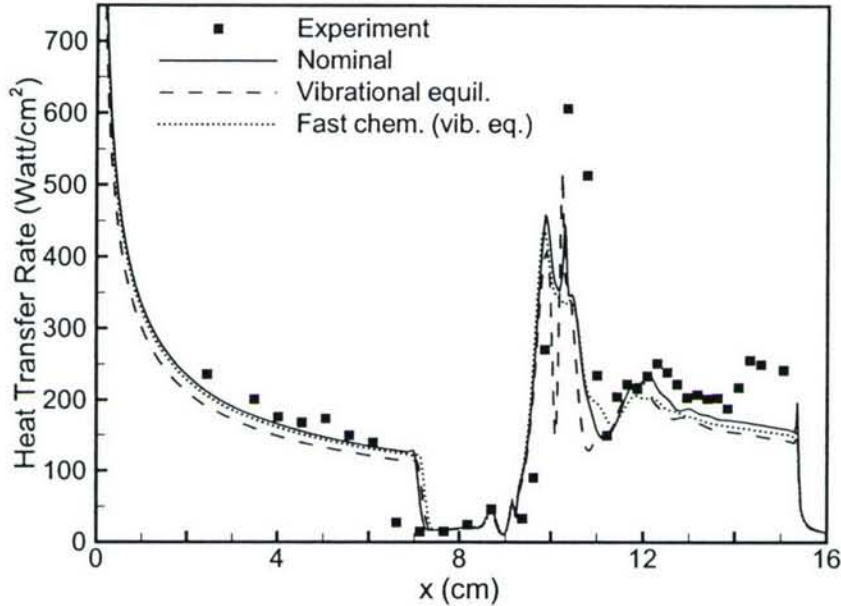


Figure 6. Computed heat transfer rate to the wall for Mach 10 air flow at 10 MJ/kg free-stream specific enthalpy.

Calculations of double-cone flows in high enthalpy air showed poor agreement. Fig. 6 shows the computed heat transfer rate results for three simulations of Mach 10 air flow at 10 MJ/kg free-stream specific enthalpy. The calculation under nominal conditions does not predict the separation zone size, and the heat flux to the wall is underpredicted even in the attached region of the flow along the first cone. The peak in heat transfer is not predicted. Bounding calculations using the fictitious super-catalytic wall condition showed only a small difference in heat flux. We would assume that any agreement with the data in this case would be spurious. Additional calculations of the double-cone flow under conditions of forced chemical equilibrium (very fast reaction rates in the computed nozzle flow) and forced vibrational equilibrium do not show improvement.

Many more air cases were simulated and similar discrepancies were observed. Figure 7 plots the heat transfer rate to the wall for three air cases (Run 59 at 4.5 MJ/kg, Run 54 at 10.4 MJ/kg, and Run 65 at 15.2 MJ/kg) which are arranged in ascending order of free-stream enthalpy. We see that as the enthalpy increases agreement worsens.

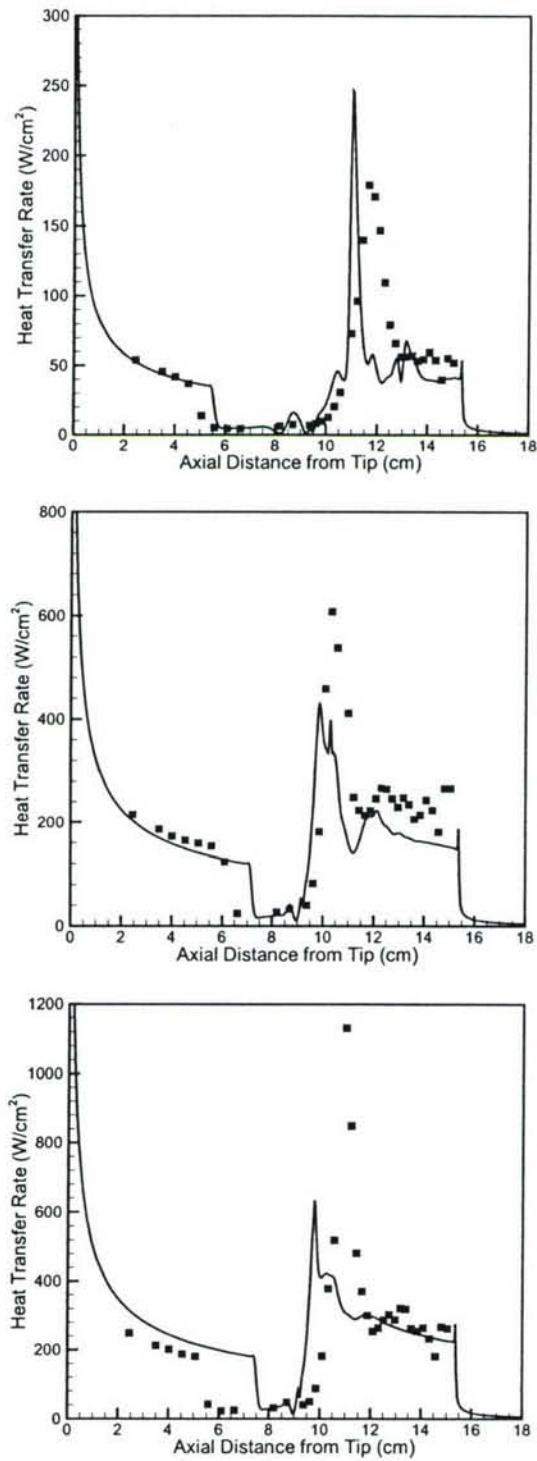


Figure 7. Predicted and measured heat transfer rate for Run 59, Run 54 and Run 65 (high enthalpy air cases ordered in terms of free-stream enthalpy).

4. Scope of the Present Work

In this work, we use computational fluid dynamics to study hypersonic double-cone experiments performed in the LENS facility at high enthalpy air. Because we are unable to explain and correct for the discrepancies that we observe between numerical predictions and the experimental measurements, we study the experiments using advanced chemistry models. We show results for high enthalpy air double-cone flows for range of conditions. These simulations utilize standard chemical kinetics models that are being used presently in hypersonic CFD applications. We also make use of results from recent work on non-intrusive diagnostics of the flow inside the nozzle. We compare the predicted nitric oxide (NO) content at the nozzle exit plane with what is inferred from laser absorption measurements made at LENS.

The following two sections of the report are included for completeness. Section 2 concerns the governing equations that are solved by the computational fluid dynamics code. The standard models that are employed in CFD are outlined. Augmentations to the baseline models to accommodate for more advanced flow physics are discussed in the relevant sections. We present the governing equations for the continuum flow of a gas in vibrational and chemical nonequilibrium. The Navier-Stokes equations for a chemically reacting and vibrationally relaxing air mixture are presented,. The numerical treatment of the equations is presented in section 3. We use standard numerical techniques which are popular among researchers and have been widely used for practical applications. It should be noted that we have validated the use of these models for the double-cone flow in earlier work. We are confident that with the numerical treatment of choice and with our previous experience in grid generation for these problems we are adequately resolving the fluid flow physics.

Section four explores the possibility of employing a detailed vibrational relaxation and diatomic molecule dissociation model based on a recent state-specific modeling formulation. The work described analyzes the sensitivity of the free-stream conditions to the level of approximation that is involved in computing vibrational relaxation and its effect on dissociation.

II. Mathematical Formulation

In this section, we introduce the set of coupled partial differential equations that describes the dynamics of the flow-field. For the high enthalpy flows of interest, the standard mass, momentum and energy equations are not sufficient to describe the thermochemical state of the gas and physics involved. The high temperatures inherent to these flows trigger a number of chemical and energy relaxation processes, or “real-gas” effects, and the flows are frequently in substantial nonequilibrium. We account for real-gas effects by introducing finite-rate chemical reactions and internal energy relaxation to the conservation equations.

The Navier-Stokes equation set has been extended so that it accurately describes the physics of a gas that is vibrationally excited and chemically reacting [Candler (1988), Olejniczak (1997)], and it is only briefly presented here. The equation of state of the gas is developed. The models used for the transfer of mass between different chemical species, transport of momentum, and the transfer of energy between different energy modes are discussed along with their underlying assumptions.

1. Basic Assumptions

The flowfields are assumed to be accurately described by a continuum formulation. For this assumption to be valid, the Knudsen number defined as the ratio of the mean free path to the length scale of the flow $\text{Kn} = \lambda/L$, must be small. For the flows of interest the Knudsen number is of the order of 0.1-0.001 based on the model size, and thus the flowfield is in the continuum regime. It is implicit in the continuum formulation that there is little statistical variation at any point in the flow and therefore the continuum description of the viscous fluxes is consistent.

We restrict the formulation to non-ionized, chemically reacting flows. The rotational state of the gas typically equilibrates within a few collisions and we can assume that the translational and rotational states of the gas are in equilibrium at a common temperature. In this work we do not consider electronic excitation of the particles.

2. The Conservation Equations

For a chemically reacting mixture of ns species, of which nd are diatomic, there are ns species mass conservation equations of the form

$$\frac{\partial \rho_s}{\partial t} + \nabla \cdot (\rho_s \vec{u}) = -\nabla \cdot (\rho_s \vec{v}_s) + w_s ,$$

where ρ_s is the density of species s , \vec{v}_s is the species diffusion velocity, and w_s is the rate of production of the species due to chemical reactions. By summing the species density over all species we get the mixture density ρ . If we sum the species mass conservation equation

over all species s , the source terms that appear on the right hand side sum identically to zero and we recover the traditional continuity equation. The models used to describe the diffusion velocities and the form of the source terms will be discussed in subsequent sections.

The conservation of linear momentum is expressed as

$$\frac{\partial(\rho\vec{u})}{\partial t} + \nabla \cdot (\rho\vec{u} \otimes \vec{u} + pI) = \nabla \cdot \tilde{\tau} ,$$

where p is the thermodynamic pressure and $\tilde{\tau}$ is the viscous stress tensor. This vector equation represents 3 momentum equations, one for each spatial dimensions of the problem. The above expression assumes that there are no external body forces exerted on the particles. Note that diffusion velocities do not appear in the momentum equation as their contributions sum identically to zero (see Olejniczak (1997) for the details of the calculation).

The conservation of total energy of the mixture is given by

$$\frac{\partial E}{\partial t} + \nabla \cdot ((E + p)\vec{u}) = \nabla \cdot (\tilde{\tau}\vec{u}) - \nabla \cdot (\vec{q}_t + \vec{q}_r + \vec{q}_v) - \nabla \cdot \sum_{s=1}^{ns} (\rho_s h_s \vec{v}_s) ,$$

where \vec{q}_t , \vec{q}_r , \vec{q}_v are the translational, rotational and vibrational heat flux vectors, and h_s is the total enthalpy per unit mass of species s . The terms present in the energy equation will be discussed separately.

In our formulation we assume that vibration-vibration energy coupling is very strong such that all vibrational modes are in equilibrium with each other. Thus the vibrational energy of the diatomic species can be described by a single vibrational temperature. This is a significant simplification as we only have one vibrational energy conservation equation, while in principle we need to have a separate equation for each of the polyatomic species. The equation for the vibrational energy per unit volume is given as

$$\frac{\partial E_v}{\partial t} + \nabla \cdot (E_v \vec{u}) = -\nabla \cdot \vec{q}_v - \nabla \cdot \sum_{s=1}^{nd} (\rho_s e_{vs} \vec{v}_s) + w_v ,$$

where e_{vs} is the vibrational energy per unit mass of species s . The source term appearing on the right hand side of the equation will be discussed in the subsequent sections.

3. Equations of State

In this section, we show how conserved variables relate to the primitive flow variables, such as temperature, and pressure that appears in the conservation equations. The total

energy per unit volume of the gas is defined as

$$E = \sum_{s=1}^{ns} \rho_s C_{vs} T + \frac{1}{2} \rho |\vec{u}|^2 + \sum_{s=1}^{nd} e_{vs} \rho_s + \sum_{s=1}^{ns} h_s^\circ \rho_s ,$$

where C_{vs} is the translational-rotational specific heat at constant volume for species s , and is given by

$$C_{vs} = C_{vs}^{(tr)} + C_{vs}^{(rot)} .$$

The translational and rotational specific heats are given by

$$C_{vs}^{(tr)} = \frac{3}{2} \frac{R}{M_s}$$

$$C_{vs}^{(rot)} = \frac{R}{M_s} \quad s \leq nd ,$$

where R is the universal gas constant and M_s is the species molecular weight. Thus the first term in the energy corresponds to the internal energy of the gas due to thermal translational-rotational motion of particles. The second term represents the bulk kinetic energy of the gas. The third term represents the vibrational energy of the polyatomic species. The vibrational energy per unit mass e_{vs} of species s is related to the vibrational temperature T_v assuming a Boltzmann distribution exists. In this work, we use a simple harmonic oscillator model to represent the vibrational excitation of diatomic species and this internal energy is expressed as

$$e_{vs} = \frac{R}{M_s} \frac{\theta_{vs}}{\exp(\theta_{vs}/T_v) - 1} ,$$

where θ_{vs} is the characteristic temperature of vibration for species s . Note that it is not possible to solve this equation directly for T_v , and therefore the vibrational temperature must be computed iteratively for a given vibrational energy $E_v = \sum_{s=1}^{nd} \rho_s e_{vs}$. The final term in the expression for the total energy represents the chemical energy of formation associated with each species.

The thermodynamic pressure p is related to the translational-rotational temperature through a perfect gas law and is obtained by Dalton's Law of partial pressures of the species as

$$p = \sum_{s=1}^{ns} p_s = \sum_{s=1}^{ns} \rho_s \frac{R}{M_s} T = \rho \bar{R} T, \quad \text{and} \quad \bar{R} \equiv \sum_{s=1}^{ns} \frac{\rho_s}{\rho} \frac{R}{M_s} .$$

The enthalpy per unit mass of species s is defined to be

$$h_s = C_{vs} T + \frac{p_s}{\rho_s} + e_{vs} + h_s^\circ .$$

4. The Diffusive Terms

In this section we describe the viscous, thermal and mass diffusion fluxes that appear in the conservation equations, and their constitutive relations.

The viscous stress tensor is formed assuming a Newtonian fluid and is given by

$$\tilde{\tau} = \mu(\nabla \vec{u} + (\nabla \vec{u})^T) + \lambda(\nabla \cdot \vec{u})I ,$$

with the Stokes hypothesis for the bulk viscosity

$$2\mu + 3\lambda = 0 ,$$

where μ is the kinematic viscosity of the mixture. The viscosity μ depends on the state of the fluid and its composition and will be discussed in detail below.

The heat fluxes are assumed to obey Fourier's Law and given by

$$\vec{q}_i = -\kappa_i \nabla T_i ,$$

where i represents *any* of the internal energy modes of the gas, with κ_i and T_i the corresponding conductivity and temperature. Since the translational and rotational states of the gas are in equilibrium at a common temperature, it is convenient to combine the corresponding heat fluxes into a sum of the conductivities times the temperature gradient as

$$\vec{q} = \vec{q}_t + \vec{q}_r = -(\kappa_t + \kappa_r) \nabla T .$$

The thermal conductivities for the translational, rotational, and vibrational energy modes are determined from an Eucken relation [Vincenti and Kruger (1986)] as

$$\kappa_{ts} = \frac{5}{2} \mu_s C_{vs}^{(tr)} , \quad \kappa_{rs} = \mu_s C_{vs}^{(rot)} , \quad \kappa_{vs} = \mu_s C_{vs}^{(vib)} ,$$

where μ_s and κ_s are the species viscosities and thermal conductivities. The vibrational specific heat is computed directly using

$$C_{vs}^{(vib)} = \frac{\partial e_{vs}}{\partial T_v} .$$

Mass diffusion is driven by gradients of concentration, pressure, and temperature. However, for the flows of interest only the terms due to concentration gradients are significant. Thermal diffusion is important in regions where gradients are large, but in these regions the fundamental continuum assumption is typically invalid and we can no longer

apply the Navier-Stokes equations [Boyd *et al.* (1995)]. The baro-diffusion terms are negligible. Therefore, for this work the mass diffusion is solely based on concentration gradients and Fick's Law is used. The mass diffusion flux is

$$\rho_s \vec{v}_s = -\rho \mathcal{D}_s \nabla \left(\frac{\rho_s}{\rho} \right) .$$

The multicomponent diffusion coefficients \mathcal{D}_s are replaced with a single binary diffusion coefficient \mathcal{D} , which is derived assuming a constant Lewis number, Le , defined as

$$\text{Le} = \mathcal{D} \frac{\rho C_p}{\kappa} ,$$

where C_p is the translational-rotational specific heat at constant pressure and κ is the thermal conductivity of the mixture. The effects of multicomponent diffusion have been neglected, however they should be included if light species, such as hydrogen, are present in the flow.

It now remains to provide expressions for the mixture viscosity, the thermal conductivity and the species viscosities. The mixture viscosity μ and thermal conductivity κ are obtained from the species viscosities and conductivities μ_s , κ_s using Wilke's semi-empirical mixing rule [Wilke (1950)]

$$\mu = \sum_s \frac{X_s \mu_s}{\phi_s} , \quad \kappa = \sum_s \frac{X_s \kappa_s}{\phi_s} ,$$

where

$$X_s = \frac{c_s M}{M_s} , \quad M = \left(\sum_s \frac{c_s}{M_s} \right)^{-1} ,$$

$$\phi_s = \sum_r X_r \left[1 + \sqrt{\frac{\mu_s}{\mu_r}} \left(\frac{M_r}{M_s} \right)^{1/4} \right]^2 \left[\sqrt{8 \left(1 + \frac{M_s}{M_r} \right)} \right]^{-1} ,$$

and $c_s = \rho_s / \rho$ is the mass fraction of species s . The model of Blottner is used for the species viscosities μ_s , which are calculated from curve fits of the form

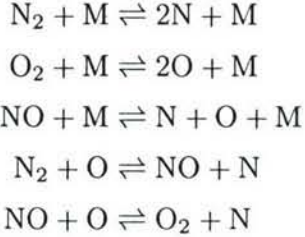
$$\mu_s = 0.1 \exp[(A_s \ln T + B_s) \ln T + C_s] ,$$

where A_s , B_s , and C_s are constants. This model is valid for a large range of temperature (to about 10,000 K), and is suitable for this work.

5. The Chemical Source Terms

Each of the source terms w_s that appear in the mass conservation equations represents the rate of production and destruction of species s due to chemical reactions. In this section we present the chemical source terms that appear in the mass conservation equations.

In the high enthalpy flows that we examine in this work, two different gases are used: nitrogen and air. The treatment of nitrogen can be considered as a special case of the air gas, and thus the set of conservation equations for nitrogen flows is a subset of the equation set that describes air flows. For high temperature air with no ionization, there are five chemical reactions that are important, involving five species: N_2 , O_2 , NO , N , and O . The chemical reactions involved are



The reactions are presented so that they are endothermic in the forward direction. The first three reactions represent dissociation of the diatomic species N_2 , O_2 , and NO due to collisions. In these reactions, M is arbitrary and represents the collision partner which provides the energy to break the chemical bond. The three corresponding reverse reactions are three-body recombination, during which the collision partner M absorbs the energy released during the formation of chemical bonds. The two remaining reactions are the Zeldovich exchange reactions, which are the primary source of nitric oxide (NO) in a hypersonic flow.

The rates of the forward and backward reactions take an Arrhenius form governed by the forward and backward rate coefficients k_{frm} and k_{brm} respectively. We may write the rate of each reaction as a sum of the forward and backward rates

$$\begin{aligned} \mathcal{R}_1 &= \sum_m \left[k_{b1m} \frac{\rho_{\text{N}}}{M_{\text{N}}} \frac{\rho_{\text{N}}}{M_{\text{N}}} \frac{\rho_{\text{m}}}{M_{\text{m}}} - k_{f1m} \frac{\rho_{\text{N}_2}}{M_{\text{N}_2}} \frac{\rho_{\text{m}}}{M_{\text{m}}} \right] \\ \mathcal{R}_2 &= \sum_m \left[k_{b2m} \frac{\rho_{\text{O}}}{M_{\text{O}}} \frac{\rho_{\text{O}}}{M_{\text{O}}} \frac{\rho_{\text{m}}}{M_{\text{m}}} - k_{f2m} \frac{\rho_{\text{O}_2}}{M_{\text{O}_2}} \frac{\rho_{\text{m}}}{M_{\text{m}}} \right] \\ \mathcal{R}_3 &= \sum_m \left[k_{b3m} \frac{\rho_{\text{N}}}{M_{\text{N}}} \frac{\rho_{\text{O}}}{M_{\text{O}}} \frac{\rho_{\text{m}}}{M_{\text{m}}} - k_{f3m} \frac{\rho_{\text{NO}}}{M_{\text{NO}}} \frac{\rho_{\text{m}}}{M_{\text{m}}} \right] \\ \mathcal{R}_4 &= k_{b4} \frac{\rho_{\text{NO}}}{M_{\text{NO}}} \frac{\rho_{\text{N}}}{M_{\text{N}}} - k_{f4} \frac{\rho_{\text{N}_2}}{M_{\text{N}_2}} \frac{\rho_{\text{O}}}{M_{\text{O}}} \\ \mathcal{R}_5 &= k_{b5} \frac{\rho_{\text{O}_2}}{M_{\text{O}_2}} \frac{\rho_{\text{N}}}{M_{\text{N}}} - k_{f5} \frac{\rho_{\text{NO}}}{M_{\text{NO}}} \frac{\rho_{\text{O}}}{M_{\text{O}}} \end{aligned}$$

The chemical source terms can now be expressed in terms of the individual reaction rates

$$\begin{aligned} w_{\text{N}_2} &= M_{\text{N}_2} (\mathcal{R}_1 + \mathcal{R}_4) \\ w_{\text{O}_2} &= M_{\text{O}_2} (\mathcal{R}_2 - \mathcal{R}_5) \\ w_{\text{NO}} &= M_{\text{NO}} (\mathcal{R}_3 - \mathcal{R}_4 + \mathcal{R}_5) \\ w_{\text{N}} &= M_{\text{N}} (-2\mathcal{R}_1 - \mathcal{R}_3 - \mathcal{R}_4 - \mathcal{R}_5) \\ w_{\text{O}} &= M_{\text{O}} (-2\mathcal{R}_2 - \mathcal{R}_3 + \mathcal{R}_4 + \mathcal{R}_5) \end{aligned}$$

We note that the sum of all the source terms is identically zero, so that conservation of total mass is satisfied, and elemental conservation of atomic nitrogen and oxygen is also satisfied.

The forward and backward reaction rate coefficients are in general affected by the level of thermal nonequilibrium in the flow. In this work we use the model of Park (1986) for vibration-dissociation coupling. The Park model has been used extensively, since it is simple to implement and has been shown to give satisfactory results for a variety of flow conditions [Olejniczak (1997)]. The Park model assumes that the reaction rates are functions of an effective temperature, and therefore we represent the forward reaction rate coefficients by the modified Arrhenius form

$$k_{f_m} = C_{f_m} T_{\text{eff}}^{\eta_m} \exp(-\theta_m/T_{\text{eff}}) ,$$

where C_{f_m} , η_m , and θ_m are found from curve fits to experimental data. In this work, the values recommended by Park (1988) are used. The effective temperature T_{eff} that appears in the expression is some function of the translational-rotational and vibrational temperatures. Park recommends that the geometric average of the translational and vibrational temperatures is used for the forward rates of the dissociation reactions, as

$$T_{\text{eff}} = \sqrt{TT_v} .$$

The backward reaction rate coefficients are related to the forward reaction rate coefficients through the equilibrium constant defined as their ratio

$$K_{\text{eq}_m}(T) = \frac{k_{f_m}(T_{\text{eff}})}{k_{b_m}} .$$

The equilibrium constant, K_{eq} , is also a curve fit to experimental data, and is a function only of T

$$K_{\text{eq}_m} = C_m \exp(A_{1m} + A_{2m}Z + A_{3m}Z^2 + A_{4m}Z^3 + A_{5m}Z^4) ,$$

where $Z = 10,000/T$. The constants that appear in the expression for K_{eq_m} are given by Park (1985).

6. Vibrational Energy Source Term

The source term that appears on the right hand side of the vibrational energy equation (w_v) is presented here. This source term is due to the exchange of energy between the translational-rotational and vibrational modes of the gas. Additionally, the creation of diatomic molecules, due to recombination reactions, contributes to the vibrational energy source term.

There are many energy exchange mechanisms between the different internal energy modes of the gas, including exchange between translational and vibrational modes, exchange between rotational and vibrational modes, and exchange between vibrational modes of the separate species. In this work, we have assumed that the vibration-vibration exchanges are very fast, and thus the vibrational modes of the gas are in equilibrium at the same vibrational temperature T_v . The vibration-translation and vibration-rotation energy exchange rates are combined in a single energy exchange rate Q_{t-v} , and the Landau-Teller model is used [Vincenti and Kruger (1986)]. The energy exchange rate is given as

$$Q_{t-v}^{(LT)} = \rho_s \frac{e_{vs}^* - e_{vs}}{\langle \tau_s \rangle} ,$$

where e_{vs}^* is the vibrational energy per unit mass of species s evaluated at the translational temperature (equilibrium), and $\langle \tau_s \rangle$ is the molar averaged Landau-Teller relaxation time, and is given by Lee (1985) as

$$\langle \tau_s \rangle = \frac{\sum_r X_r}{\sum_r X_r / \tau_{sr}} ,$$

where X_r has been defined previously and τ_{sr} is Landau-Teller inter-species relaxation time given by Millikan and White (1963), as

$$\begin{aligned} \tau_{sr} &= \frac{1}{p} \exp[A_{sr}(T^{-1/3} - 0.015\mu_{sr}^{1/4}) - 18.42] , \quad (p \text{ in atm}) \\ A_{sr} &= 1.16 \times 10^{-3} \mu_{sr}^{1/2} \theta_{vs}^{4/3} , \\ \mu_{sr} &= \frac{M_s M_r}{M_s + M_r} . \end{aligned}$$

Part of the vibrational energy source terms is due to the creation and destruction of diatomic species in chemical reactions. For this work, we assume that the molecules that are recombining and molecules that dissociate carry vibrational energy given by the local vibrational temperature. Therefore, the rate of production of vibrational energy due to chemical reactions is just

$$Q_{vs} = w_s e_{vs} .$$

The vibrational energy source term w_s is simply the sum of the contributions of the two processes, namely recombination and translation-vibration energy exchange, and is given by

$$w_v = \sum_{s=1}^{nd} Q_{t-v}^{(LT)} s + \sum_{s=1}^{nd} w_s e_{vs} .$$

III. Numerical Method

In this section we present the numerical method we use to solve the coupled partial differential equations that describe the flows of interest. The conservation laws presented in the previous section were expressed in their strong form. However, we obtain numerical solutions to this set of conservation equations by considering the weak form of the equations. We use a standard finite volume method to discretize the governing equations in the approximation space.

We introduce the finite volume formulation, and the methods we use to evaluate the inviscid and viscous terms. The implicit method employed for time advancement is also briefly presented. We will restrict the remaining of this section to the two-dimensional case in order to simplify the calculations, but it should be noted that it is straightforward to extend the numerical method to three dimensions.

1. The Finite Volume Method

In this section, we introduce the finite volume method of discretization. We begin with the strong form of the equations presented in the previous section. We write the vector of conserved variables as

$$U = (\rho_1, \dots, \rho_{\text{ns}}, \rho u, \rho v, E_v, E)^T ,$$

and the conservation equations can now take the compact form

$$\frac{\partial U}{\partial t} + \nabla \cdot \vec{F} = W ,$$

where \vec{F} is the corresponding total flux vector and W is the vector of source terms

$$W = (w_1, \dots, w_{\text{ns}}, 0, 0, w_v, 0)^T .$$

The total flux can be split into the convective (inviscid) and diffusive flux vectors

$$\vec{F} = \vec{F}_I + \vec{F}_v .$$

The Cartesian components of the convective and diffusive flux vectors are

$$F_I = \begin{pmatrix} \rho_1 u \\ \rho_2 u \\ \vdots \\ \rho_{\text{ns}} u \\ \rho u u + p \\ \rho v u \\ E_v u \\ (E + p) u \end{pmatrix} , \quad G_I = \begin{pmatrix} \rho_1 v \\ \rho_2 v \\ \vdots \\ \rho_{\text{ns}} v \\ \rho u v \\ \rho v v \\ E_v v \\ (E + p) v \end{pmatrix} ,$$

$$F_v = \begin{pmatrix} \rho_1 u_1 \\ \rho_2 u_2 \\ \vdots \\ \rho_{ns} u_{ns} \\ -\tau_{xx} \\ -\tau_{xy} \\ q_{v_x} + \sum_{s=1}^{nd} (\rho_s e_{v_s} u_s) \\ q_x + q_{v_x} - (\bar{\tau} \vec{u})_x + \sum_{s=1}^{ns} (\rho_s h_s u_s) \end{pmatrix},$$

$$G_v = \begin{pmatrix} \rho_1 v_1 \\ \rho_2 v_2 \\ \vdots \\ \rho_{ns} v_{ns} \\ -\tau_{yx} \\ -\tau_{yy} \\ q_{v_y} + \sum_{s=1}^{nd} (\rho_s e_{v_s} v_s) \\ q_y + q_{v_y} - (\bar{\tau} \vec{u})_y + \sum_{s=1}^{ns} (\rho_s h_s v_s) \end{pmatrix}.$$

In the finite volume formulation, the weak form of the conservation equations is obtained by integrating over an arbitrary control volume Ω , which, for the purposes of this work, is assumed to be fixed in space. Green's Theorem is applied to convert the volume integral containing the flux vector, to a surface integral over the surface that encloses Ω . The resulting weak form of the equation is

$$\frac{\partial \bar{U}}{\partial t} + \frac{1}{V} \oint_{\partial\Omega} (\vec{F} \cdot \hat{n}) dS = \bar{W},$$

where V is the total volume, \hat{n} is the outward-pointing normal to the surface, and \bar{U} , \bar{W} are averaged over Ω . We discretize physical space by dividing it into a series of volume elements, which can be arbitrary polygons. We do this by building a regular mesh over the domain of interest, resulting in a structured grid. The grid directions are defined such that i index increases in the ξ -direction and j increases in the positive η -direction. Each of the volume elements in the two-dimensional domain is a quadrilateral, and represents a cell in computational space. Flow variables are stored at the cell centers rather than the nodes. Quantities at the cell faces are computed from the solution reconstruction based on the cell-centered data. The time rate of change of \bar{U} in the 2-D volume element i,j is represented as a sum of the fluxes over the four cell faces and the generation of U within

the volume

$$\begin{aligned} \frac{\partial \bar{U}_{i,j}}{\partial t} = & -\frac{1}{V_{i,j}} \left[(\vec{F} \cdot \hat{n})_{i+\frac{1}{2},j} S_{i+\frac{1}{2},j} - (\vec{F} \cdot \hat{n})_{i-\frac{1}{2},j} S_{i-\frac{1}{2},j} \right. \\ & \left. + (\vec{F} \cdot \hat{n})_{i,j+\frac{1}{2}} S_{i,j+\frac{1}{2}} - (\vec{F} \cdot \hat{n})_{i,j-\frac{1}{2}} S_{i,j-\frac{1}{2}} \right] + \bar{W}_{i,j} . \end{aligned}$$

The $\pm 1/2$ indices on the flux and surface area terms indicate that quantities should be evaluated at the appropriate cell face. This expression is the discretized form of the conservation equations for a two-dimensional domain. The extension of the formulation to three dimensions, where the volume elements are hexahedra, is straight-forward and results in an analogous expression. The axisymmetric formulation, however, is non-trivial, and ultimately yields an expression similar to that of the two-dimensional case. Integrating the conservation equations over an axisymmetric domain introduces extra terms that appear as sources in the forcing vector W .

2. Evaluation of the Fluxes

In this section we present the methods we use for evaluating the fluxes that appear on the right hand side of the discretized form of the conservation equations. We have decomposed the fluxes into the convective part (which consists of the advection terms and the pressure) and diffusive part. This decomposition is useful because we treat the convective and diffusive fluxes differently. The inviscid terms make the system of equations hyperbolic, while the viscous terms are diffusive in nature, and make the system parabolic when combined with the transient term. This complicates the evaluation of the right hand side of the conservation equations. The elliptic nature of the diffusive terms allows for a simple central difference scheme to be used [Hirsch (1991)]. A more sophisticated approach is necessary for the calculation of the inviscid terms, in order to maintain stability of the numerical scheme.

In the computation of the inviscid terms, we make use of the fact that in hyperbolic systems of equations, information propagates along definable characteristic directions in space-time. This is commonly referred to as upwind biasing. We employ a modified form of the Steger-Warming (1981) flux-vector splitting, a method widely used due to its robustness, which is based on characteristic theory. We present the application of this method specifically to the set of conservation equations relevant to this work (see also Wright (1997)), but it should be noted that the method has been implemented for more

complex sets of conservation equations. We consider the inviscid flux through a face

$$F'_I = \vec{F}_I \cdot \hat{n} = \begin{pmatrix} \rho_1 u' \\ \rho_2 u' \\ \vdots \\ \rho_{ns} u' \\ \rho u u' + p s'_x \\ \rho v u' + p s'_y \\ E_v u' \\ (E + p) u' \end{pmatrix}$$

where s'_x, s'_y are the components of the unit vector normal to the surface in question, and u' is the component of the velocity normal to the surface. We observe that the flux F'_I is linear and homogeneous in the vector of conserved variables U , i.e.,

$$F'_I(\lambda U) = \lambda F'_I(U) ,$$

where λ is an arbitrary scalar. This can be shown if we express the inviscid flux F'_I in terms of the components of U . The homogeneity of the flux allows us to express it exactly in terms of the linearization

$$F'_I(U) = \frac{\partial F'_I}{\partial U} U = A' U ,$$

where A' is the inviscid flux Jacobian matrix in the direction of \hat{n} . We follow the approach of Steger and Warming to split the inviscid fluxes into positively-moving and negatively-moving components using an upwind biasing scheme. The partitioning is performed by diagonalizing A' , and the fluxes are split according to the sign of the eigenvalues of the Jacobian. The diagonalization of $\frac{\partial F'_I}{\partial U}$ is rather cumbersome, but we can simplify the operation by breaking the Jacobian into components, as

$$A' = \frac{\partial U}{\partial V} \frac{\partial V}{\partial U} \frac{\partial F'_I}{\partial V} \frac{\partial V}{\partial U} ,$$

where V is a vector of primitive variables, introduced for convenience. The choice of V is not unique, but for the particular inviscid fluxes it is convenient to use

$$V = (\rho_1, \rho_2, \dots, \rho_{ns}, u, v, e_v, p)^T ,$$

where e_v is the total vibrational energy per unit mass. The transformation matrices between primitive and conservative variables are denoted by S^{-1} and S . We should, in principle, be able to diagonalize using a similarity transformation

$$\frac{\partial V}{\partial U} \frac{\partial F'_I}{\partial V} = C_{A'}^{-1} \Lambda_{A'} C_{A'} ,$$

where $\Lambda_{A'}$ is a diagonal matrix of eigenvalues, $C_{A'}^{-1}$ is the matrix of eigenvectors of A' , and $C_{A'}$ such that $C_{A'}^{-1}C_{A'} = I$. The diagonalization process has now been simplified, however the resulting expressions for the eigenvectors, although mathematically correct, may exhibit singularities and are not suitable for use in a numerical algorithm. Therefore, we introduce an orthogonal transformation R , which transforms the momenta from a coordinate system locally aligned with the face in question, to the Cartesian system. We can now write the Jacobian matrix as

$$A' = S^{-1}R^{-1}C_A^{-1}\Lambda_{A'}C_A R S ,$$

where C_A does not exhibit singularities. The diagonal components of $\Lambda_{A'}$ are the convection speeds of the characteristic variables. The flux vector can now be split into the positively and negatively moving components defined by

$$\begin{aligned} F'_+ &= S^{-1}R^{-1}C_A^{-1}\Lambda_+C_A R S U = A'_+ U \\ F'_- &= S^{-1}R^{-1}C_A^{-1}\Lambda_-C_A R S U = A'_- U , \end{aligned}$$

where Λ_+ and Λ_- are the split eigenvalue matrices consisting of the positive and negative eigenvalues respectively. The total inviscid flux vector through the face in question can be expressed as the sum of positively and negatively moving components

$$F'_I = F'_+ + F'_- .$$

In this basic discretization, the split fluxes at each cell face are evaluated using

$$\begin{aligned} F'_{+i+\frac{1}{2},j} &= A'_{+i,j} U_{i,j} , \\ F'_{-i+\frac{1}{2},j} &= A'_{-i+1,j} U_{i+1,j} , \end{aligned}$$

where A'_{\pm} and U are evaluated based on the upwind cell data. MacCormack and Candler (1989) proposed a modification to this method, which reduces the amount of numerical dissipation of the original method. Their modification suggests that the Jacobian matrix should be evaluated at the cell face, rather than using the upwind cell data. This approach works well in regions of weak gradients, but additional dissipation is required to capture strong gradients and shock waves. In this work, we use a hybrid method, in which we use pressure weighted average quantities between adjacent cells to evaluate the Jacobian. The method smoothly switches from modified to true Steger-Warming in regions of large pressure gradients. This flux evaluation method as originally formulated is only first order accurate in space, however it is possible to achieve higher order of accuracy. Higher order accurate schemes can produce more resolved solutions on a given computational mesh. We use up to second order accurate fluxes in this work. We obtain higher order of accuracy by

extrapolating the conserved variables to the cell face based on the purely upwind cell data. We detect the presence of shock waves by identifying pressure jumps greater than 50% of the smallest pressure involved in the flux evaluation stencil, in which case we switch the stencil to first order. For the details of this formulation see Druguet *et al.* (2003).

If we substitute the split fluxes into the discretized form of the conservation equations, we get the upwind finite volume formulation of the inviscid equations

$$\begin{aligned} \frac{\partial \bar{U}_{i,j}}{\partial t} = -\frac{1}{V_{i,j}} & \left[\left(A'_{+i+\frac{1}{2},j} S_{i+\frac{1}{2},j} U_{i,j} - A'_{+i-\frac{1}{2},j} S_{i-\frac{1}{2},j} U_{i-1,j} \right) \right. \\ & - \left(A'_{-i-\frac{1}{2},j} S_{i-\frac{1}{2},j} U_{i,j} - A'_{-i+\frac{1}{2},j} S_{i+\frac{1}{2},j} U_{i+1,j} \right) \\ & + \left(B'_{+i,j+\frac{1}{2}} S_{i,j+\frac{1}{2}} U_{i,j} - B'_{+i,j-\frac{1}{2}} S_{i,j-\frac{1}{2}} U_{i,j-1} \right) \\ & \left. - \left(B'_{-i,j-\frac{1}{2}} S_{i,j-\frac{1}{2}} U_{i,j} - B'_{-i,j+\frac{1}{2}} S_{i,j+\frac{1}{2}} U_{i,j+1} \right) \right] + \bar{W}_{i,j}, \end{aligned}$$

where we have implicitly defined A' and B' to denote the inviscid flux Jacobians in the ξ and η directions respectively.

The elliptic nature of the viscous fluxes makes their evaluation possible with a simple finite difference scheme. The viscous flux vector is evaluated at the required cell faces using central differencing. The viscous fluxes integrated over a face take the simple form

$$\begin{aligned} F'_{v,i+\frac{1}{2},j} S_{i+\frac{1}{2},j} &= (\vec{F}_v \cdot \hat{n})_{i+\frac{1}{2},j} S_{i+\frac{1}{2},j} \\ G'_{v,i,j+\frac{1}{2}} S_{i,j+\frac{1}{2}} &= (\vec{F}_v \cdot \hat{n})_{i,j+\frac{1}{2}} S_{i,j+\frac{1}{2}}. \end{aligned}$$

The contribution of the viscous fluxes is summed over the four cell faces and added to the right hand side of the discretized form of the conservation equations. The required derivatives that appear in the viscous fluxes are taken with respect to the general curvilinear coordinate system ξ - η , and are then transformed to the Cartesian system. The calculation of these terms can be found in Hirsch (1991).

3. Time Advancement

In this section we discuss how the solution is integrated in time to its steady state. We are interested solely in the steady state solution, if one exists, and thus time accuracy is not important for our computations. Therefore, we employ an implicit method, which allows for large time steps to be taken, while maintaining stability of the numerical scheme. We give a short description of the implicit formulation here. We first introduce the explicit method of solution, and then we extend it to the implicit formulation.

We discretize the transient term that appears in the conservation equations, in order to time-march the solution toward the steady state. We use simple first-order Euler backward

differencing, in which the time derivative becomes

$$\frac{\partial U_{i,j}}{\partial t} = \frac{U_{i,j}^{n+1} - U_{i,j}^n}{\Delta t} + \mathcal{O}(\Delta t^2) \simeq \frac{\Delta U_{i,j}^n}{\Delta t}$$

and the superscript denotes the time level in the temporal discretization. This expression is substituted directly into the discretized form of the conservation equations, and the solution is marched forward in time by discrete time steps. The explicit formulation of the inviscid problem is

$$\begin{aligned} \Delta U_{i,j}^n = -\frac{\Delta t}{V_{i,j}} & \left[\left(A'_{+i+\frac{1}{2},j} S_{i+\frac{1}{2},j} U_{i,j} - A'_{+i-\frac{1}{2},j} S_{i-\frac{1}{2},j} U_{i-1,j} \right) \right. \\ & - \left(A'_{-i-\frac{1}{2},j} S_{i-\frac{1}{2},j} U_{i,j} - A'_{-i+\frac{1}{2},j} S_{i+\frac{1}{2},j} U_{i+1,j} \right) \\ & + \left(B'_{+i,j+\frac{1}{2}} S_{i,j+\frac{1}{2}} U_{i,j} - B'_{+i,j-\frac{1}{2}} S_{i,j-\frac{1}{2}} U_{i,j-1} \right) \\ & \left. - \left(B'_{-i,j-\frac{1}{2}} S_{i,j-\frac{1}{2}} U_{i,j} - B'_{-i,j+\frac{1}{2}} S_{i,j+\frac{1}{2}} U_{i,j+1} \right) \right]^n + \Delta t W_{i,j}^n, \end{aligned}$$

where $\Delta U_{i,j}^n$ is the explicit change in the solution vector (residual) at cell i,j at time step n . The solution is updated to the next time level using

$$U_{i,j}^{n+1} = U_{i,j}^n + \Delta U_{i,j}^n.$$

We call this an explicit method because the solution in the next time level $n+1$, is computed explicitly by evaluating the right hand side at the current time level n . The solution at any point at time level $n+1$ is independent of the solution at other points at the same time level.

With a fully implicit method, the time-step limitations inherent to explicit solvers can be overcome. The use of an implicit solver can allow, in general, for time steps much larger than the stable explicit time step. In an implicit method, the solution at any point depends on the solution of all other points at the time level $n+1$. Therefore, in order to employ implicit time advancement, it is necessary to evaluate the right hand side of the conservation equations at time level $n+1$. We express the fluxes that appear on the right hand side in terms of the linearization

$$\begin{aligned} F_I'^{n+1} &= F_I'^n + \frac{\partial F_I'}{\partial U} \Big|_U^n (U^{n+1} - U^n) + \mathcal{O}(\Delta t^2) \\ &\simeq F_I'^n + A'^n \delta U^n \end{aligned}$$

where we have defined the vector $\delta U^n = U^{n+1} - U^n$ and we have frozen the variation of the inviscid flux Jacobian A'^n between time steps. We apply this linearization to the split

fluxes and source vector to obtain the fully implicit upwind formulation of the inviscid problem

$$\begin{aligned} \delta U_{i,j}^n + \frac{\Delta t}{V_{i,j}} & \left[\left(A'_{+i+\frac{1}{2},j} S_{i+\frac{1}{2},j} \delta U_{i,j} - A'_{+i-\frac{1}{2},j} S_{i-\frac{1}{2},j} \delta U_{i-1,j} \right) \right. \\ & - \left(A'_{-i-\frac{1}{2},j} S_{i-\frac{1}{2},j} \delta U_{i,j} - A'_{-i+\frac{1}{2},j} S_{i+\frac{1}{2},j} \delta U_{i+1,j} \right) \\ & + \left(B'_{+i,j+\frac{1}{2}} S_{i,j+\frac{1}{2}} \delta U_{i,j} - B'_{+i,j-\frac{1}{2}} S_{i,j-\frac{1}{2}} \delta U_{i,j-1} \right) \\ & \left. - \left(B'_{-i,j-\frac{1}{2}} S_{i,j-\frac{1}{2}} \delta U_{i,j} - B'_{-i,j+\frac{1}{2}} S_{i,j+\frac{1}{2}} \delta U_{i,j+1} \right) \right]^n \\ & - \Delta t C_{i,j}^n \delta U_{i,j}^n = \Delta U_{i,j}^n, \end{aligned}$$

where $C_{i,j}^n$ is the Jacobian of W with respect to U . In this implicit equation, $\Delta U_{i,j}^n$ is the explicit residual as defined previously.

We include the implicit approximation of the viscous terms in the implicit equation by applying the linearization to the viscous fluxes. We define $\delta F_v'^n$ and $\delta G_v'^n$ such that

$$\begin{aligned} F_v'^{n+1} &= F_v'^n + \delta F_v'^n \\ G_v'^{n+1} &= G_v'^n + \delta G_v'^n. \end{aligned}$$

Therefore, we only need to find expressions for $\delta F_v'$ and $\delta G_v'$. We note that F_v' and G_v' are functions of U and its spatial derivatives. The derivatives are taken with respect to the general curvilinear coordinate system, and then transformed to the Cartesian system using the operators

$$\frac{\partial}{\partial x} = \frac{\partial \xi}{\partial x} \frac{\partial}{\partial \xi} + \frac{\partial \eta}{\partial x} \frac{\partial}{\partial \eta}, \quad \frac{\partial}{\partial y} = \frac{\partial \xi}{\partial y} \frac{\partial}{\partial \xi} + \frac{\partial \eta}{\partial y} \frac{\partial}{\partial \eta}.$$

We apply the thin-layer assumption to the derivatives in the implicit viscous terms. In this way, we selectively retain derivatives depending on which viscous flux we wish to approximate. For example, in the approximation of $\delta G_v'$ we compute the derivatives by

$$\frac{\partial}{\partial x} \simeq \frac{\partial \eta}{\partial x} \frac{\partial}{\partial \eta}, \quad \frac{\partial}{\partial y} \simeq \frac{\partial \eta}{\partial y} \frac{\partial}{\partial \eta}.$$

Similarly, derivatives with respect to ξ are retained when approximating $\delta F_v'$. If we assume that the terms not involving derivatives are locally constant, we can write F_v' and G_v' as a function of the derivatives of the flow variables with respect to ξ or η only, as

$$\delta F_v' = M_\xi \frac{\partial}{\partial \xi} (\delta \mathbf{V}), \quad \delta G_v' = M_\eta \frac{\partial}{\partial \eta} (\delta \mathbf{V}),$$

and we introduce for convenience the vector of non-conserved variables

$$\mathbf{V} = (c_1, c_2, \dots, c_{ns}, u, v, e_v, T)^T.$$

The matrices M_ξ and M_η can be found in Candler (1988). We ultimately express the implicit viscous fluxes in terms of δU by mapping from $\delta \mathbf{V}$ to δU using the Jacobian $N = \frac{\partial \mathbf{V}}{\partial U}$, and we obtain the final form

$$\delta F'_v = M_\xi \frac{\partial}{\partial \xi} (N \delta U), \quad \delta G'_v = M_\eta \frac{\partial}{\partial \eta} (N \delta U),$$

We should emphasize here that all of the viscous derivatives are retained in the computation of F'_v^n and G'_v^n , and thus all of the viscous terms influence the converged solution. With this treatment of the viscous terms, the implicit equation for the inviscid problem away from solid boundaries will be unchanged if we simply replace the inviscid Jacobians A' and B' with \tilde{A} and \tilde{B} , where

$$\begin{aligned} \tilde{A}_+ &= A_+ - M_\xi N & \tilde{A}_- &= A_- + M_\xi N \\ \tilde{B}_+ &= B_+ - M_\eta N & \tilde{B}_- &= B_- + M_\eta N \end{aligned}$$

The implicit formulation involves the solution of a linear system of equations, which has a strong diagonal dominance due to the nature of the Steger-Warming Jacobians. In principle, we can solve exactly for the $\delta U_{i,j}^n$ by a direct inversion of the operator.

4. The Data-Parallel Line-Relaxation

In this section we briefly present the method of solution of the implicit equation. We use the Data-Parallel Line Relaxation method of Wright *et al.* (1998). This method was developed to take advantage of parallel computing machines, and appears to be superior to other implicit methods [Wright (1997)]. Only a brief description of this method is given here. Details on the performance of the method can be found in Wright (1997) and Wright *et al.* (1998).

The standard implicit upwind formulation of the Navier-Stokes equations for a reacting gas is essentially a linear system of equations. The solution of such system can, in principle, be obtained directly by inversion of a large block banded matrix. This becomes very computationally intensive, as such an inversion must be performed at every time step until convergence is achieved. Therefore, most implicit methods seek to make simplifications in order to make the solution of the problem less expensive. Such simplifications are possible only on the left-hand side of the equations, which resembles the *numerics*. The right-hand side of the equation (residual) should be unaltered.

It is convenient to introduce some additional notation in order to group terms on the

left-hand side of the implicit equation. We let

$$\begin{aligned}
\hat{A}_{i,j} &= \frac{V_{i,j}}{\Delta t} I + \left(A'^n_{+i+\frac{1}{2},j} S_{i+\frac{1}{2},j} - A'^n_{-i-\frac{1}{2},j} S_{i-\frac{1}{2},j} \right. \\
&\quad \left. + B'^n_{+i,j+\frac{1}{2}} S_{i,j+\frac{1}{2}} - B'^n_{-i,j-\frac{1}{2}} S_{i,j-\frac{1}{2}} \right) - V_{i,j} C_{i,j}^n \\
\hat{B}_{i,j} &= B'^n_{-i,j+\frac{1}{2}} S_{i,j+\frac{1}{2}} \\
\hat{C}_{i,j} &= B'^n_{+i,j-\frac{1}{2}} S_{i,j-\frac{1}{2}} \\
\hat{D}_{i,j} &= A'^n_{-i+\frac{1}{2},j} S_{i+\frac{1}{2},j} \\
\hat{E}_{i,j} &= A'^n_{+i-\frac{1}{2},j} S_{i-\frac{1}{2},j} .
\end{aligned}$$

We can simplify the operator if we assume that the physical problem is strongly coupled in the η direction. Then, we can move some of the off-diagonal terms to the right-hand side of the implicit equation, keeping only constant i terms on the left-hand side. In this way, it is possible to solve for all j points at each i location as a series of fully coupled block tri-diagonal systems aligned in the η direction. We relax the off-diagonal terms by updating the unknowns on the right-hand side of the equation with the $\delta U_{i,j}$ we have just computed. We do not need to obtain an exact solution to the implicit equation, but rather to maintain stability, and thus only a few iterations are required per time step. The solution procedure is as follows. First, the implicit terms on the right-hand side are neglected and the resulting block tri-diagonal system is factored and solved for $\delta U^{(0)}$ according to:

$$\hat{B}_{i,j} \delta U_{i,j+1}^{(0)} + \hat{A}_{i,j} \delta U_{i,j}^{(0)} - \hat{C}_{i,j} \delta U_{i,j-1}^{(0)} = \Delta U_{i,j}^n$$

where the superscript denotes the sub-iteration number (zero denotes the initialization). Then, a series of k_{max} relaxation steps is performed, where we solve

$$\hat{B}_{i,j} \delta U_{i,j+1}^{(k)} + \hat{A}_{i,j} \delta U_{i,j}^{(k)} - \hat{C}_{i,j} \delta U_{i,j-1}^{(k)} = -\hat{D}_{i,j} \delta U_{i+1,j}^{(k-1)} + \hat{E}_{i,j} \delta U_{i-1,j}^{(k-1)} + \Delta U_{i,j}^n ,$$

and the superscript $k - 1$ indicates that data from the previous relaxation step is used. Finally, the solution is obtained by

$$\delta U_{i,j}^{n+1} = \delta U_{i,j}^{(k_{max})} .$$

There are two advantages to this method of solution. First, the method can be implemented efficiently on a distributed memory parallel computer. This is because we can split the problem among processors in the i direction, effectively assigning a series of i -columns to each processor. Therefore, each relaxation step can be performed simultaneously as there are no data dependencies, while the boundary data can be efficiently transferred.

Secondly, there is no bias in the solution procedure, which has been shown to impose a bias in the solution itself.

5. Boundary Conditions

In this section we describe the boundary conditions used for both the explicit residual and the implicit operator, and how they are implemented in the numerical algorithm.

In the finite volume method, explicit boundary conditions are imposed using “dummy” cells. An extra layer of cells is included around the grid that represents physical space, in which variables are stored in order to impose the appropriate boundary conditions for the problem. The dummy cells are constructed in such a way that derivatives taken in terms of the curvilinear body-fitted coordinate system are consistent with the type of boundary condition of the viscous fluxes. Because we split the fluxes into the viscous and inviscid parts, we treat the boundary conditions separately.

In the explicit formulation, we simulate no-slip conditions by setting the velocity at the wall to zero, and extrapolating the velocity components at the boundary cell $i,1$ based on the values at the cell $i,2$. We simulate isothermal wall conditions in a similar fashion. The slip conditions require that we have a model for how the velocity component tangent to the wall is computed based on the interior values. The details of the model employed were presented in the previous section. Once the slip velocity has been determined, we extrapolate values to the dummy cells, as we did for the no-slip case. We impose internal energy jumps at the wall in exactly the same fashion. The non-catalyticity of the wall is imposed by setting the values of the species densities at the dummy cells equal to the interior values, effectively imposing a zero mass-fraction gradient. Similarly, fully catalytic boundary conditions are imposed by extrapolating mass-fractions to the dummy cell assuming the mass-fractions of atomic species is zero at the wall. Subsequently, the mass flux of polyatomic species at the wall is corrected such that we have elemental conservation during this process.

The implicit treatment of the boundary conditions is analogous to that of the explicit method. In the implicit formulation, however, it is not the variables at dummy cells that are set to a certain value, but their effect on the implicit operator which we construct. Specifically, the boundary conditions are folded into the implicit operator by making a modification to the $\hat{A}_{i,j}$ matrix where appropriate. For example, the inviscid boundary conditions at the wall are included by adding the matrix $\hat{C}_{i,2}E_w$ to $\hat{A}_{i,2}$, where $\hat{C}_{i,j}$ was defined previously, and E_w is an operator that reflects the momentum normal to the wall. Similarly, the approximate implicit viscous Jacobian M_η is modified at solid boundaries. The details of the implicit treatments of boundaries are described in Candler (1988) and Gökçen (1989). Note that the viscous wall implicit boundary conditions are folded into

the block matrix $\hat{A}_{i,2}$ and should not be included in $\hat{C}_{i,2}$.

6. Other Flux Evaluation Methods

The inviscid flux evaluation method discussed earlier is one of many methods suitable for gas dynamic simulations. There are several methods used widely in numerical algorithms, and these are of variable degree of sophistication and complexity. Different flux evaluation methods exhibit different properties in terms of accuracy and computational cost. Most importantly, the amount of numerical dissipation that is associated with a numerical scheme depends largely on the choice of flux evaluation and solution reconstruction methods. In general, a scheme with little numerical dissipation produces more accurate results on a given computational mesh.

It is beyond the scope of this work to make comparisons between different flux evaluations methods. However, it is important to assess how well the numerical method of choice performs in comparison with other methods. Therefore, a later section discusses in more detail results of simulations made using several other methods of evaluating the inviscid fluxes. These flux evaluation methods are not covered in great detail, and are only presented briefly.

7. Second Order Spatial Accuracy

Higher order accurate inviscid fluxes can be obtained through appropriate reconstruction of the solution using cell-centered data. Based on the choice of the reconstruction method, the accuracy of the inviscid fluxes may differ. In this section, we briefly present the methods used in this work.

The flux evaluation method discussed previously is first order accurate when data from adjacent cells are used to calculate the flux. The method can become second order accurate with a simple modification. Consider the Steger-Warming flux for the inviscid equations in one spatial dimension:

$$F = F_+(U_i) + F_-(U_{i+1}) .$$

In this form, the split fluxes use upwind data from adjacent cells. A higher order numerical flux H may be obtained if we replace the arguments of F_+ and F_- with a left state U^L and a right state U^R as:

$$\begin{aligned} H &= F_+(U^L) + F_-(U^R) \\ &= A_+U^L + A_-U^R , \end{aligned}$$

where U^L and U^R are extrapolated conserved quantities based on pure upwind data. It should be noted that this simple extrapolation is not suitable for regions of the flow that

exhibits large gradients in U , such as shock waves. Therefore, we need to detect the presence of a shock, and use no extrapolation in that case. Our implementation uses pressure jumps across cell faces in order to detect the presence of shocks, as discussed earlier.

The MUSCL variable extrapolation method may also be used to construct higher order Steger-Warming and modified Steger-Warming fluxes. In this case, the left and right states U^L, U^R are constructed based on non-linear functions of the ratio of adjacent slopes of U computed based on cell-centered data. Details on slope limiters and their use in the MUSCL variable extrapolation can be found in Hirsch (1991) and Laney (1998).

IV. Detailed Vibrational Relaxation and Dissociation Modeling

In this subsection we present work that was done exclusively on nitrogen flows. This work aims to address modeling issues associated with vibrational relaxation, its effect on dissociation, and the sensitivity of double-cone flows to these aspects of the chemistry modeling. We do not concern ourselves with the numerical treatment of the equations that are solved, and the focus is solely on the physical modeling.

We believe that from a modeling perspective it is easier to investigate the high enthalpy nitrogen cases. Furthermore, it makes sense to focus our efforts on the nitrogen flows, for which we obtained very good agreement under low enthalpy conditions. Therefore, in the present work we build on the previous modeling efforts to study the CUBRC LENS high enthalpy nitrogen flows.

We show results of vibrational relaxation in nitrogen using the latest state-specific models available in the literature for vibrational energy relaxation through quantum transitions. We emphasize that although the equation set is very complex, the uncertainty in the rates that accompany the model are the key source of uncertainty in the numerical predictions. We use recently developed models for multi-quantum state-specific vibration-translation (V-T) and vibration-vibration (V-V) relaxation rates in simulations of the expanding high enthalpy flow in the nozzle. Parametric studies of the sensitivity of the free-stream conditions to modeling of the V-T and V-V relaxation rates are presented. The results show that the free-stream conditions are nearly insensitive to detailed vibrational relaxation modeling under these conditions and that with possible minor modifications the traditional Landau-Teller model is sufficient. The reason for the discrepancies observed between the present high enthalpy experiments and simulations is not explained from our findings here.

1. Computational Method

The standard conservation equations have been modified to implement the state-specific model of vibrational relaxation. In the case of state-specific modeling of nitrogen molecules, each vibrational state is treated as a different chemical species, and thus a separate mass conservation equation is solved for each vibrational state. The diatomic species are ordered in terms of the energy that is associated with each of the vibrational states. For nitrogen, this results in having $n_v + 1$ mass conservation equations, where n_v is the number of vibrational quantum states considered; the additional equation is due to the nitrogen atoms present in the flow. Note that we do not include all 46 vibrational states of nitrogen, because the equations would be too expensive to solve on an adequate grid. However, using fewer levels than 46 is adequate as will be shown in subsequent subsections. We use the Park rates for the Arrhenius-type dissociation reactions, and the

reverse reactions are calculated using Park's fits for the equilibrium constants. The details of the physical modeling are discussed in detail in the following subsection.

2. Vibrational State-Specific Modeling

One of the major uncertainties in the prediction of high-enthalpy nozzle flows is how to model the coupled vibrational relaxation and recombination. As the gas expands through the nozzle, the vibrational modes relax by vibration-translation (V-T) and vibration-vibration (V-V) collisional processes. At the same time, the atoms recombine to form new molecules. These molecules may be formed with large vibrational energy; this energy is then redistributed by V-T and V-V relaxation. This process has been modeled by many different authors, including Bray (1968, 1970), Treanor *et al.* (1968), Center and Caledonia (1972), Ruffin (1995a, 1995b), and Josyula and Bailey (2004). This work shows that anharmonic effects are important, as well as the competition between the rates of the different processes. Ruffin's work is notable in that full master equation simulations of hypersonic nozzle flows show excellent agreement with experiments.

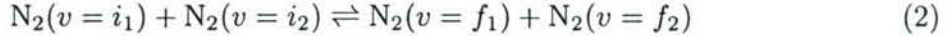
In this work, we use recently developed models for multi-quantum state-specific vibration-translation (V-T) and vibration-vibration (V-V) relaxation rates [Adamovich (1997, 1998)]. These closed-form rate models are the most accurate currently available, and have been compared to experimental data and detailed quantum mechanical calculations. We model the expanding gas using a state-specific approach, representing each vibrational state as a separate chemical species at each point in the flow. Each of the vibrational species can react with another via V-T and V-V processes as the gas expands in the nozzle. We also include a separate species for nitrogen atoms to allow V-T relaxation of the N_2 molecules by atoms. The atoms are allowed to recombine according to appropriate rate models.

The standard nozzle flow analysis code uses a simple Landau-Teller relaxation model for the vibrational energy modes. Recombination is modeled conventionally, with a single rate obtained from the dissociation rate and the equilibrium constant. As discussed in previous work, we use the Spalart-Allmaras single-equation turbulence model for the nozzle boundary layer, and we compute from the reservoir through the throat to the test section. For the LENS-Leg I nozzle with 1.125" inch diameter throat, we use a 1007×128 grid which has been shown to give grid-converged results.

We want to make *direct* comparisons between higher fidelity modeling approaches and the standard model. Therefore, we use the same grid and turbulence model for all simulations. The forced harmonic oscillator (FHO) model of Adamovich *et al.* (1997) is used with multi-quantum V-T and V-V transitions allowed. The V-T reaction is written



where M is any collision partner. The V-V process is



Thus in principle, an N_2 molecule can transition from any vibrational state to any other vibrational state by either of these mechanisms. Therefore, for a full state-specific model of N_2 (with 46 levels), this is a very costly simulation on an adequate grid. We can reduce the cost of the simulation by only considering near-resonant V-V processes and limiting the allowed change in the vibrational quanta.

The modeling of the recombination process is unclear because we must specify the nascent vibrational state of the recombining molecules. Most previous work assumes that only the uppermost vibrational level is active in the reactive processes. This approach is based on the ladder-climbing model of dissociation which is not relevant in hypersonic nozzle flows.

We can obtain some guidance from previous quasi-classical trajectory analysis [Bose, *et al.* (1997)] of the exothermic Zeldovich reaction $O_2 + N \rightarrow NO + O$. In that work, the nascent NO vibrational state was tracked for a range of reactant vibrational and translational states. It was found that the molecules tend to be formed at low vibrational states. To a first estimate, the product molecules are equally distributed across the lower 15 vibrational quanta, with a significant reduction in the population beyond that level. Thus, at least for this reaction, the molecules are more likely to be formed at the low vibrational levels. With this observation in mind, we can develop two different modeling approaches for the product vibrational state.

First consider strict detailed balancing; here we assume that the equilibrium constant for each state's population must hold. In this case, we have in equilibrium (denoted by *)

$$K_{eq}(v) = \frac{[N]^* [N]^*}{[N_2(v)]^*} = \frac{[N]^* [N]^*}{[N_2]^*} \frac{[N_2]^*}{[N_2(v)]^*} \quad (3)$$

Since we know the equilibrium constant for the N_2 dissociation and the equilibrium Boltzmann distribution, we can determine $K_{eq}(v)$. This approach effectively distributes the product molecules to the vibrational energy pool based on the local Boltzmann distribution. This favors population of the low levels, and it clearly satisfies detailed balance.

A second approach is to use the results of the Zeldovich reaction analysis discussed earlier, and assume that the molecules are equally disposed to the vibrational states. Then the expression for the equilibrium constant becomes

$$K_{eq}(v) = \frac{[N]^* [N]^*}{[N_2]^*} \frac{1}{n_v} \quad (4)$$

where n_v is the number of vibrational states being modeled. It is not clear that such a formulation satisfies detailed balance; however if the V-T and V-V rates are relatively fast, the gas will reach an equilibrium governed by a Boltzmann.

2. State-Specific Modeling Results

Non-Reacting Results

First let us consider a pure N₂ gas expanding from the reservoir conditions given by $T_o = 6720\text{ K}$, $\rho_o = 8.680\text{ kg/m}^3$, $c_N = 0.02647$. If we run the state-specific code and the single vibrational temperature Landau-Teller model, we should get very similar results. As shown in Table 1, this is the case with the state-specific code giving essentially the same results as the baseline code. The only difference should be due to using the anharmonic oscillator model in the state-specific simulations. In addition, the vibrational energy distribution function is Boltzmann at the nozzle exit, as required by the model. In this state-specific simulation, 10 vibrational levels were used; we will show that this is sufficient to represent this flow.

Table 1 also presents the results for state-specific simulations using the forced harmonic oscillator model rate expressions for single quantum V-T transitions and for a full multi-quantum V-T model with nearest neighbor V-V transitions. The FHO rates are faster than the Millikan and White expression for the Landau-Teller relaxation model, so the state-specific simulations give more rapid equilibration. This is shown in Fig. 8, which plots the FHO and Millikan and White rates for the $v = 1$ to $v = 0$ V-T transition. The faster FHO rates result in a lower test-section vibrational temperature and a correspondingly higher velocity. Somewhat surprisingly, the multi-quantum V-T and the nearest-neighbor V-V processes do not have an appreciable effect on the vibrational relaxation. This results in essentially no difference in the predicted free-stream conditions.

Reacting Results

Initial simulations with the two possible recombination models showed little difference. Therefore, the detailed-balance model was used for all of the simulations presented here. Figure 8 shows that the V-T rate for N atom collisions is an order of magnitude faster than the molecule-molecule rate. Thus we expect that N atoms will increase the vibrational relaxation process. Also, as the atoms recombine, they release energy which increases the flow energy.

Table 1. Simulation results for non-reacting nozzle flows for reservoir conditions corresponding to equilibrium at $T_o = 6720\text{ K}$, $\rho_o = 8.680\text{ kg/m}^3$ and 100% N_2 . Vibrational temperature based on lowest two levels.

	Baseline	State-Specific Landau-Teller	State-Specific FHO Single-Quantum V-T	State-Specific FHO Multi-Quantum + V-V
$u(\text{m/s})$	3933	3918	3946	3946
$\rho(\text{g/m}^3)$	1.491	1.503	1.481	1.481
$T(\text{K})$	285.0	296.7	296.7	296.7
$T_v(\text{K})$	3086	3037	2732	2731
p_{Pitot}	23130	23140	23110	23110
c_{N_2}	1.0	1.0	1.0	1.0

Table 2. Simulation results for reacting nozzle flows for reservoir conditions corresponding to equilibrium at $T_o = 6720\text{ K}$, $\rho_o = 8.680\text{ kg/m}^3$ and 97.35% N_2 by mass.

	Baseline	State-Specific FHO Multi-quant.	State-Specific V-T	State-Specific Multi-quant., 16 levels	State-Specific V-T + V-V ($\Delta v = \pm 1$)	State-Specific V-T + V-V ($\Delta v = \pm 2$)
$u(\text{m/s})$	4108	4137		4149	4127	4126
$\rho(\text{g/m}^3)$	1.407	1.388		1.381	1.393	1.393
$T(\text{K})$	321.5	344.6		348.6	342.6	342.4
$T_v(\text{K})$	3168	2535		2544	2536	2536
p_{Pitot}	21900	23840		23850	23800	23800
c_{N_2}	0.9952	0.9962		0.9960	0.9952	0.9962

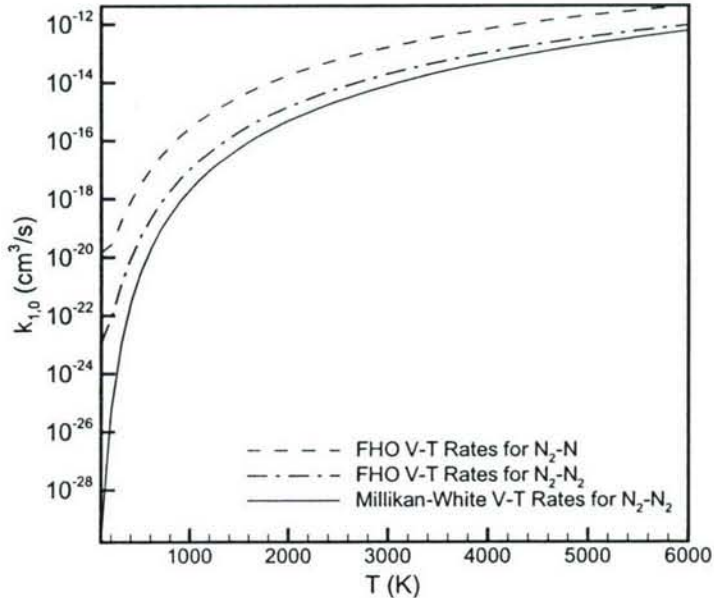


Figure 8. Plot of the vibrational-translational relaxation rate for N_2 ($v = 0 \rightarrow v = 1$) computed using the Landau-Teller model with Millikan-White fits and FHO model.

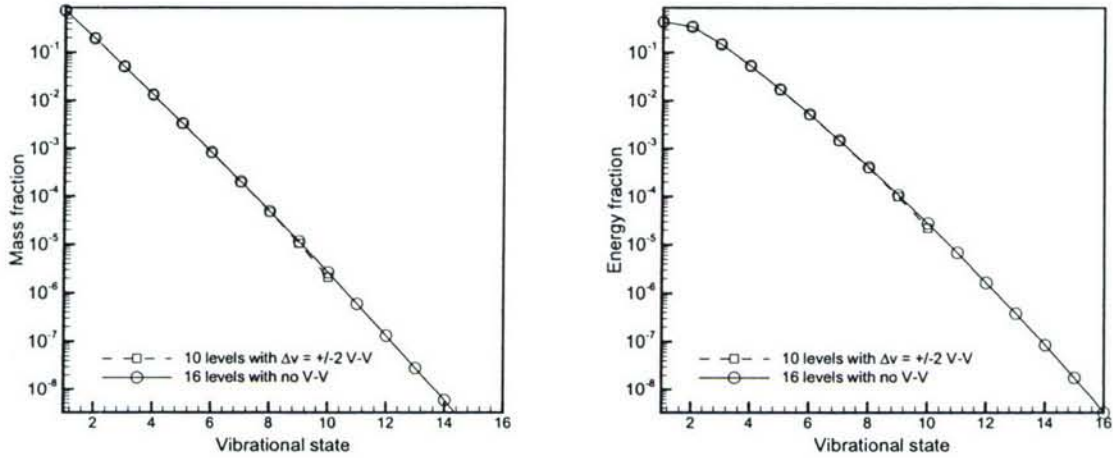


Figure 9. Distribution of the vibrational energy among states for a 10 level calculation and a 16 level calculation plotted in terms of the mass fraction (left) and energy fraction (right).

As shown in Table 2, in general, the reacting results are similar to those presented above. However, there is one obvious difference: as expected, the N atoms increase the relaxation rate and lower the predicted test-section vibrational temperature. The additional energy mostly goes into increasing the free-stream kinetic energy.

Interestingly, the V-V rates have very little effect on the flow conditions. Even when V-V transitions that have $\Delta v = \pm 2$, there is little effect of V-V processes. The tabulated results also show that the model with 10 vibrational levels is sufficient to capture the energetics of the flow. Increasing the number of levels modeled to 16 results in no appreciable change. This result is further quantified in Fig. 9, which plots the vibrational population distribution at the exit of the nozzle for the 10 and 16 level models. Figure 9 also plots the energy-weighted distribution function at the same location; note that almost all of the energy is represented by the first few levels for this flow.

These results are somewhat in contrast with those presented in previous work. However, they are the first to use the recently-developed forced harmonic oscillator rates which are more accurate than previous rate models. Clearly under the conditions considered here, the nearest-neighbor V-T processes dominate the recombination. Also, the recombination of atoms without favoring the upper levels has a significant effect on the vibrational energy distribution function in the nozzle flow.

Interestingly, Fig. 9 also shows that the vibrational energy modes are in a Boltzmann distribution at the nozzle exit. This is contrary to much of the previous literature on

hypersonic nozzle expansions which predict a complicated vibrational energy distribution function. (See Ruffin (1995a) for a clear discussion.) Again, this is a result of the dominant role of the V-T rates predicted by the FHO rate model and the non-preferential disposal of the recombination energy.

All of this complicated flow modeling results in a relatively simple conclusion: The simple Landau-Teller single vibrational temperature model will work well for high-enthalpy nozzle flows if the Millikan and White relaxation rates are adjusted to fit the modern V-T rate data. Of course this conclusion applies to pure nitrogen flows only. Ultimately, for the prediction of nozzle conditions in a hypersonic wind tunnel, the main issue is the correct prediction of the rate of energy release from the vibrational and chemical energy modes. Subtle differences in the upper vibrational state populations have little effect on the macroscopic flow parameters that are required for high-quality aerodynamic testing. Having made that broad generalization, it remains to be seen how air recombines from a high-enthalpy reservoir condition, which will be the subject of future studies.

3. Double-Cone Flow Results

In this subsection we present results from simulations of high enthalpy double-cone flows. Following the discussion of the detailed nozzle flow simulations, we present results obtained under several of the computed free-stream conditions presented earlier, as well as additional cases taken from Wadhams, *et al.* (2003). It should be noted that all of the double-cone predictions presented here were obtained using the baseline simple harmonic oscillator (SHO) model for vibration with the L-T relaxation model. Table 3 summarizes the free-stream conditions for which results are shown in this subsection.

Table 3. Summary of free-stream conditions for which simulations over the double-cone model were performed.

	Run 42 (nominal)	Run 42 (computed)	Run 42 (computed)	Run 42 (computed)	Run 46 (nominal)	Run 46 (computed)	Run 50 (nominal)	Run 40 (nominal)
	SHO L-T	FHO $v-t$	FHO $v-t v-v$		SHO L-T			
$u(\text{m/s})$	3849	4106	4137	4126	3945	4229	3904	3104
$\rho(\text{g/m}^3)$	1.468	1.407	1.388	1.393	1.958	1.839	1.509	2.530
$T(\text{K})$	268.7	321.1	344.6	342.4	281.7	347.1	272.5	172.0
$T_v(\text{K})$	2947	3170	2535	2536	3072	3083	3143	2617
c_{N_2}	1.0000	0.9952	0.9952	0.9962	0.9984	0.9960	0.9984	1.0000

The initial simulations of high enthalpy nitrogen cases (Runs 42 and 46) presented in Nompelis, *et al.* (2003a) were performed under the nominal free-stream conditions, but also under free-stream conditions computed with CFD by expanding the flow in the LENS nozzle from reservoir conditions. The nominal and computed conditions were very

similar, and simulations under both sets of conditions gave very similar results (less than 5% difference in heat transfer rates for nitrogen). For the purposes of this discussion we will refer to these results as “nominal.” Recently, the reservoir conditions for these runs were re-evaluated as presented in MacLean, *et al.* (2005), and a separate set of reservoir conditions was proposed. The newly proposed free-stream conditions suggest an increase of nearly 10% in the enthalpy for the high enthalpy nitrogen case (Run 42). All results presented here were obtained from the proposed reservoir conditions, where the free-stream was computed via nozzle flow analysis.

Figure 10 plots the surface pressure and heat transfer rate to the model for Run 42. The computed conditions from Table 1 obtained by expanding the reservoir conditions using the baseline model were used for this simulation. Under these conditions, the size of the separation zone is under-predicted by a substantial amount, resulting in overall poor agreement. However, agreement is better for the pressure in the attached flow region along the first cone and inside the separation zone.

Figure 11 shows heat transfer rate results computed under the free-stream conditions of Table 2 obtained using the more physically accurate models: the state-specific FHO model with multi-quantum V-T processes but neglecting V-V transitions, and the state-specific FHO model with multi-quantum V-T relaxation and V-V transitions of the nearest ± 2 states. The baseline result is also plotted for reference. The results worsen when the free-stream conditions obtained using the more accurate model are used. Also, the results are mutually consistent, because the computed free-stream conditions of Table 2 are very similar.

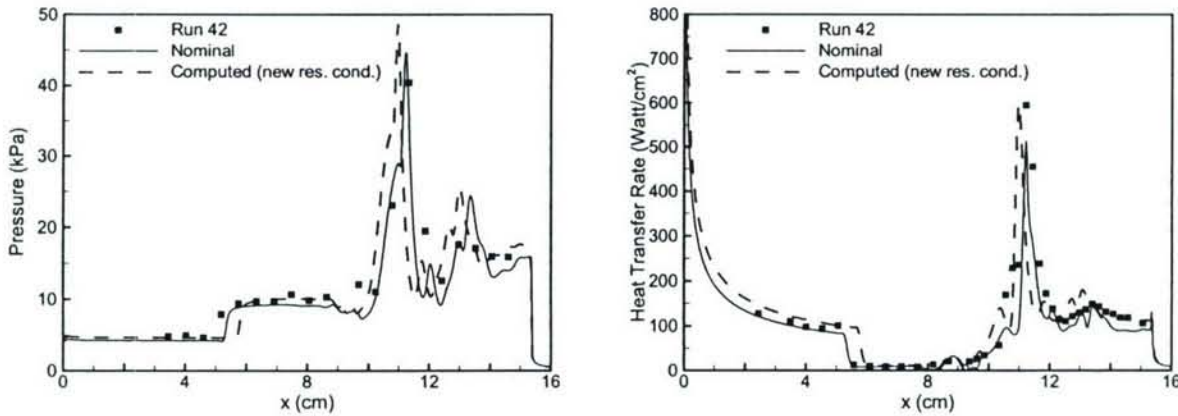


Figure 10. Numerical predictions and experimental measurements for Run 42. The computed conditions using the baseline model from Table 2 were used for this simulation; the results under nominal conditions are plotted for reference.

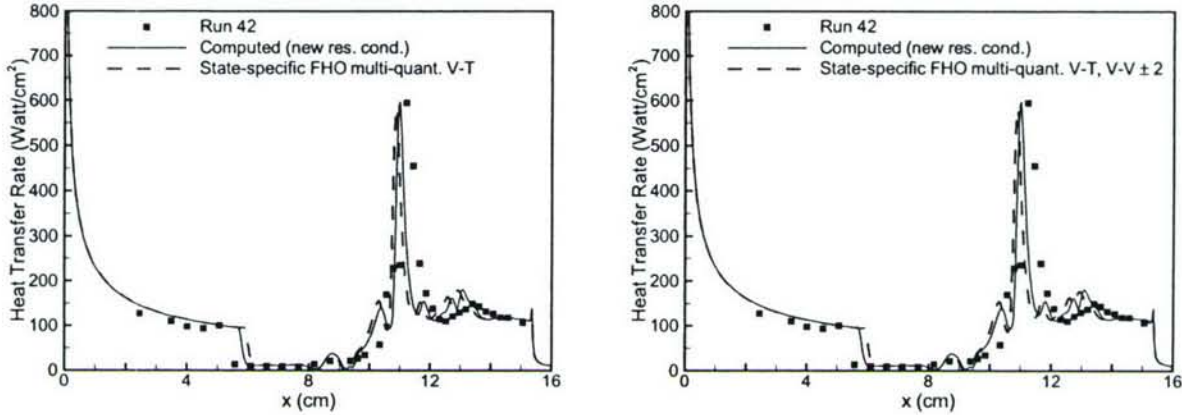


Figure 11. Comparison of predicted heat transfer rate for Run 42 using the state-specific FHO multi-quantum V-T model, and the state-specific FHO multi-quantum V-T model with V-V transitions for the nearest ± 2 states. Results under nominal conditions are plotted for reference.

Figure 12 shows results for Run 46 conditions computed from the new reservoir conditions. The size of the separation zone is substantially under-predicted under the new conditions obtained with the baseline model. However, the level of pressure along the first cone and in the separated region matches the measured values. There is an overall increase in the heat transfer rate predictions, which is closer to the experimental values along the first cone, but the agreement is still poor at reattachment. It is interesting to note that although the predicted heat transfer rate increased consistently along the entire surface of the model, there is still a large difference at the peak and after reattachment. Also, if we examine the shear layer that forms at the edge of separation and characterize it in terms of a Reynolds number as defined in Birch and Keyes, we see that for Run 46 this quantity runs dangerously close to the transition criterion specified by the authors. They compute the free shear-layer Reynolds number based on the high-speed side as: $Re_s = \rho vs/\mu$, where s is the length along the shear layer. This is shown in Fig. 13, which plots the shear layer Reynolds number for this case along with Runs 42, 43 and the low-enthalpy case Run 35. Although this dimensionless quantity is below the transition criterion, it has a trend that indicates the flow might be unsteady. Based on these results, we believe that it is likely that this case is transitional, and thus it is not useful for the purposes of this study.

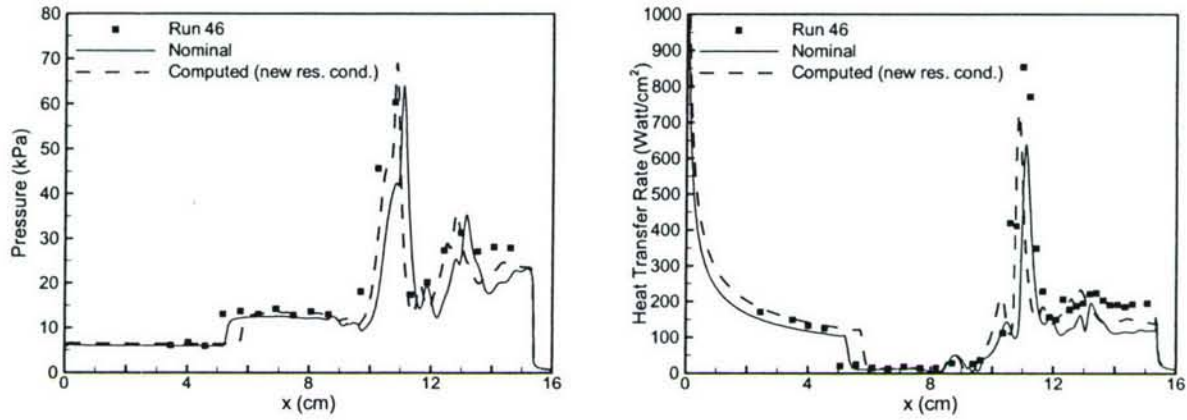


Figure 12. Numerical predictions and experimental measurements for Run 46. The computed conditions using the baseline model from Table 2 were used for this simulation; the results under nominal conditions are plotted for reference.

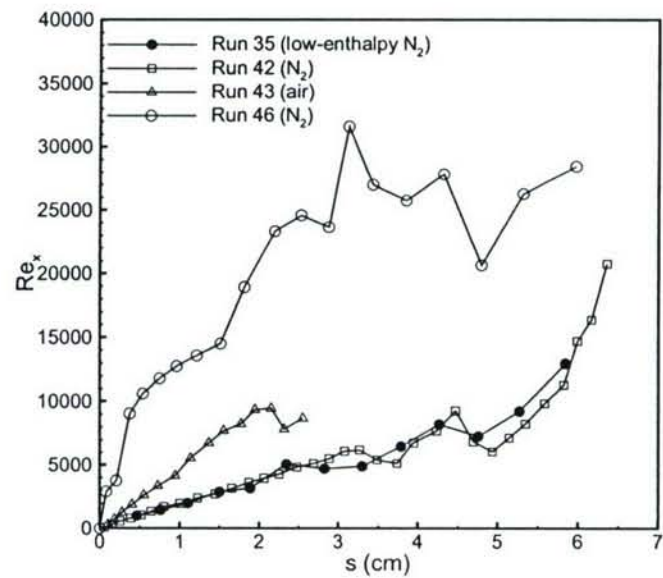


Figure 13. Free shear-layer Reynolds number for Run 46, Run 42, Run 43 (air case) and Run 35 (low enthalpy case).

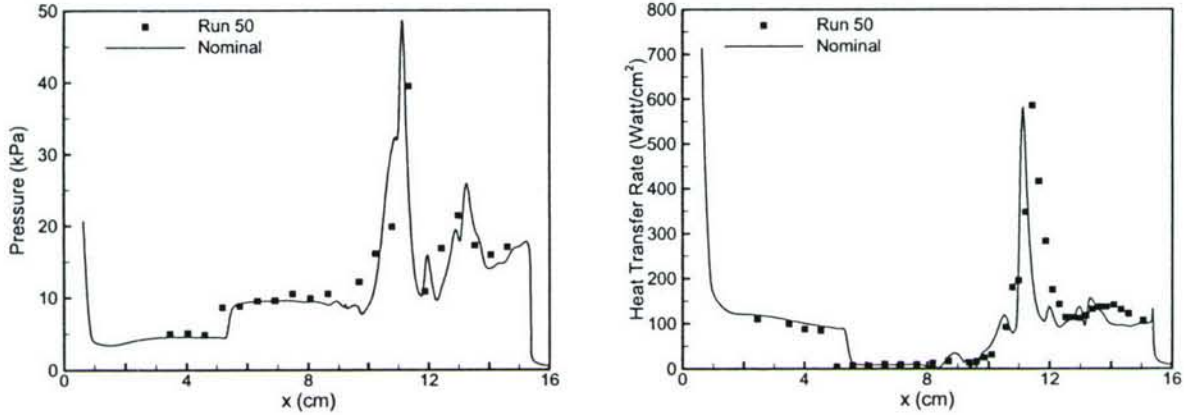


Figure 14. Computed surface pressure and heat transfer rate for Run 50 (blunt double-cone in 10 MJ/kg nitrogen).

We also simulated the flow over a blunted double-cone model in a high enthalpy nitrogen flow (Run 50). Run 50 is nominally the same as Run 42, and was included in the LENS experiments to assess the effect that a blunted nose has on the flow. The blunted nose has a strong stagnation at the model tip, which forms a large entropy layer that extends into the separation zone. Chemical effects in the entropy layer may possibly alter the flowfield, therefore it is important to know how this effect changes the basic flowfield. The simulation results along with the experimental data for this case are plotted in Fig. 14. We see good agreement for the surface pressure and heat transfer rate along the first cone, however the size of the separation is under-predicted substantially. This is a surprising result because the free-stream and reservoir conditions for Run 50 are nearly identical to Run 42 and the CFD results for both cases are very similar. However, this is not reflected in the experimental measurements.

Finally, we simulated the flow over the double-cone model under the nominal free-stream conditions of Run 40, which is a moderate enthalpy case nominally at 5 MJ/kg. This case exhibits large scale unsteadiness as predicted by the simulation, in contrast to what is seen in the experiments. This is shown in Fig. 15, which plots the heat transfer rate to the model for Run 40. The separation zone extends almost over the entire length of the geometry and is unsteady.

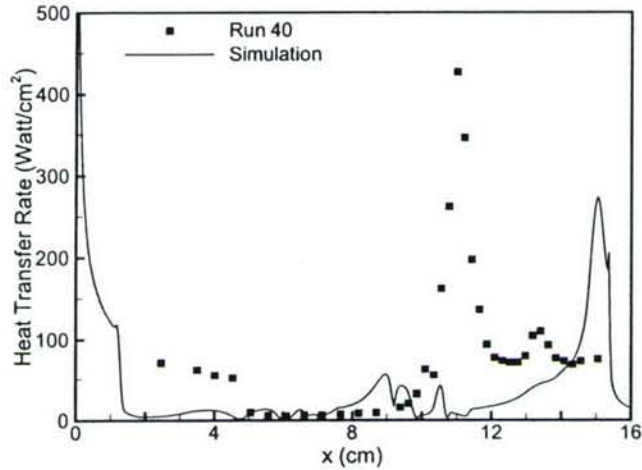


Figure 15. Computed surface heat transfer rate for Run 40.

We have simulated high enthalpy experiments in nitrogen performed in the LENS facility using the LENS Leg I tunnel. We have studied the experiments by performing simulations of the nozzle flow, expanding the reservoir conditions from the throat into the test-section. We studied Run 42 extensively using the most recently developed models for vibrational relaxation, including V-T and V-V relaxations processes. We demonstrated that for the flows of interest the free-stream conditions are not very sensitive to the models of the relaxation process and that the standard SHO model with the L-T model for relaxation gives accurate results.

We also investigated the effect of bluntness on the high enthalpy double-cone flow by simulating two different experiments at the same conditions for a sharp and a blunted double-cone model. The CFD results were very similar for the two experiments, but this was not reflected in the experimental measurements. The size of the separation zone was larger for the blunted case. The reason for this difference is unknown, and a more detailed analysis is needed to answer this question, as well as additional experiments to verify this trend experimentally.

Finally, from this study we were unable to identify the main reason for the discrepancies between experiments and simulations that was observed initially, and in fact with the proposed reservoir conditions the agreement was worse. We believe that the proposed reservoir conditions are not accurate.

V. Nozzle Flow Analysis with Non-intrusive Diagnostics

In view of the poor agreement that we have observed for high enthalpy air experiments with double-cone geometries, we shifted focus to analyzing the nozzle flow for strong nonequilibrium effects that may result in incorrectly inferring the free-stream conditions. The experimental group has invested a lot of resources in establishing a non-intrusive methodology for making measurements inside the nozzle for certain flow quantities, such as nitric oxide (NO) content. In this subsection we present work that was done in an effort to interpret the recent NO content measurements made at LENS. It should be noted that the levels of NO that are reported by the experimental group in Parker *et al.* (2006) are lower than we predict with CFD calculations under the same conditions. This work summarizes the methodology and key findings.

In this work we re-examine the nozzle flow, including the newest runs, to understand these measurements. To do so, we study the chemical reaction mechanisms that take place in the nozzle in order to explain the reason behind the elevated level of NO that is predicted with CFD compared to what is measured experimentally. We compare the physical models that we employ to the more detailed models employed by Park for conical nozzle flow simulations at similar conditions [Park (2006)].

1. Modeling Assumptions and Overview

The high enthalpy LENS experiments performed in support of the code validation study were done at nominally 5, 10 and 15 MJ/kg free-stream specific enthalpies. These conditions correspond to flight Mach numbers of about 10, 15, and 17 respectively. At these conditions (above 5 MJ/kg), when the air gas stagnates, the temperature rises to high levels, where dissociation and internal energy excitation take place. These processes are modeled in CFD. The models employed in CFD codes and for inferring the free-stream conditions make use of published data. Models are employed for calculating the rates at which energy relaxation among different modes takes place. Models are also employed to account for the distribution of energy in the different modes for each species, and how the different modes interact with each other. Although the physical models may allow for different energy modes to be out of equilibrium, the basic assumption is that all the states for a given energy mode are in equilibrium and that a Boltzmann distribution exists. Vibrational, electronic and rotational are the energy modes that are relevant for the conditions of interest in addition to the translational mode.

In this section we discuss the modeling assumptions that support the methodology employed in CFD, and the calculations of the nozzle flow. Vibrational relaxation, chemical reaction rates, dissociation, recombination and the distribution of nascent states for

recombining molecules are discussed.

Thermochemical Equilibrium in the Reservoir

In the LENS experiments, shock waves heat the test gas to high enthalpy, and then the gas expands through the throat into the nozzle to high Mach number. During this process, the gas spends sufficient time in the reservoir to reach thermochemical equilibrium. When the stagnant gas reaches equilibrium at high enthalpy conditions, part of the total enthalpy is stored in the form of chemical energy via the existence of radicals (atomic species) and nitric oxide (NO). Other species – such as N_2O – are also created but they exist in negligible amounts under these conditions. Internal energy modes of the gas are excited, and a portion of the energy is stored in vibrational and electronic energy modes. With increasing total enthalpy, a larger portion of the energy is stored in chemical form when the gas is stagnant and in thermochemical equilibrium. Table 4 shows how the total energy is distributed among the different energy modes when the gas is stagnant at different conditions.

Table 4. Distribution of the total enthalpy in the reservoir for different conditions at $p = 500$ atm.

h_o	5 MJ/kg	10 MJ/kg	15 MJ/kg
T (K)	3780	6085	7897
Thermal	77.6%	64.7%	58.3%
Vibrational	13.8%	11.8%	9.6%
Chemical	8.6%	23.4%	32.1%

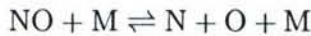
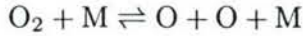
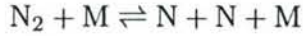
The test-gas in the reservoir remains in equilibrium at a state that is assumed not to change with time throughout the useful test-time of the experiment. Measurements are made in the reservoir to help measure the useful test-time window. The shock heated gas expands to high Mach number in the nozzle. During the sudden expansion, the gas is in a nonequilibrium state and energy relaxation and recombination of the dissociated species occur in the nozzle. This process is not well understood and we believe that it is not adequately described by the air-chemistry models that are presently employed. This is the subject of investigation in the present work. The chemical reaction rates and their underlying assumptions are discussed below.

Vibrational Energy Modes and Relaxation

It has been shown that vibrational energy relaxation plays an important role for the low enthalpy LENS experiments [Nompelis (2003)]. Vibrational energy is accounted in the CFD methodology by including a vibrational energy equation that is solved at every point in the flow. The distribution of vibrational energy is described by a simple harmonic oscillator (SHO) model for each of the diatomic species. In reality, the vibrational mode has a number of quantum states that are characteristic for each species. A conservation equation may be considered for the population of each state, but such a calculation would require accurate knowledge of the state-to-state and state-specific V-T transitions and would result in a large set of conservation equations. Because most of the energy is concentrated on the first excited state, the SHO model appears to be adequate for these flows. Detailed studies of vibrational relaxation for high enthalpy nitrogen flows in the LENS facility accounting for neighboring and near-neighboring state transitions have been performed. These simulations showed that the detailed models had little effect on the computed free-stream conditions [Nompelis (2005)]. For vibrational relaxation with the translational-rotational mode (V-T) we assume the Landau-Teller model is valid.

Chemical Reactions

Chemical reactions take place when the flow is in chemical nonequilibrium. The chemical reactions that are important in these flows are dissociation and recombination of diatomic species (N_2 , O_2 , NO) which take the form:



where M is a generic collision partner, and the Zeldovich reactions:



The total rate of reaction for each of these processes is the sum of the forward and the backward reaction rates. The reaction rate coefficients k_f and k_b that appear in the rate expressions are functions of temperature, they are different for each reaction, and in the case of dissociation reactions they are different for each collision partner M . Expressions for the rate coefficients are taken from the literature. The parameters that appear in the functional form of the rate constants are typically obtained experimentally and are valid for a range of temperatures. Typically, only the form of the forward reaction rate

coefficient k_f is given in the literature. The backward rate coefficient is calculated by using the *principle of detailed balance*.

It is assumed that the reaction moves in one direction or another based on what the composition and the state of the gas are relative to equilibrium. The composition at equilibrium is a thermodynamic property of a mixture of pure products and reactants involved in a reaction and is a function of the thermodynamic state of the mixture. Using the equilibrium constant K_{eq} the following relationship is used as a result of detailed balance:

$$K_{\text{eq}} = \frac{k_f}{k_b}$$

Published data exist for determining the equilibrium constant K_{eq} . It should be noted that the principle of detailed balance holds under the assumption that the reaction is a one-step process from products to reactants. Therefore, the calculation of the backward rate coefficient is only phenomenological.

Coupling of Reactions and Energy Modes

Because the chemical reactions are a result of collisions between particles, the reaction rate coefficients are functions of temperature. However, in the case of dissociation, a given dissociating molecule may be in any vibrational state. Thus, if diatomic molecules are on average at a high vibrational energy (elevated T_v), on average, more collisions will result in dissociation, and this is because more molecules exist close to their dissociation limit. Several models have been formulated to account for this effect. In the present work the model of Park is used which modifies the temperature at which the forward reaction rate coefficients are evaluated to use a geometric average $\sqrt{T T_v}$. This is a simple means of accounting for the effect of elevated vibrational energy in dissociation. The backward rate coefficient for dissociation reactions is not calculated based on the geometric temperature and thus it does not depend on T_v .

When atoms recombine, a molecule is created with a finite amount of energy. The energy of the particle accounts for the sum of the translational-rotational, electronic and vibrational energies. Because we use a macroscopic description of the recombination process, we assume that the nascent molecules are created at all possible vibrational states following an equilibrium distribution at the local T_v . Since electronic energy is neglected, the remaining energy is assumed to be distributed in translation-rotation in an equilibrium distribution.

It has been speculated that molecules may recombine at excited electronic states. In particular, long-lived diatomic and atomic oxygen at excited electronic states may exist in the reservoir. These energetic particles may interact with other species such that they

participate in recombination and the Zeldovich-type reactions in a preferential direction. These effects have not been considered in previous studies of the LENS experiments.

2. CUBRC LENS-I Nozzle Flow Diagnostics

Parker et al. used infrared laser energy absorption to measure the velocity, temperature and nitric oxide mass fraction at the exit plane of the CUBRC LENS-I nozzle [Parker *et al.* (2006), (2007)] The NO rotational transition at 5447nm was used for the measurements. The Doppler shift of the absorption feature gives an accurate means of measuring the gas velocity, while the width of the feature gives an estimate of the gas temperature using the HITRAN 2K database of line shapes. Then with the temperature known, the absolute concentration of nitric oxide can be computed with the assumption that the rotational and vibrational modes are in a Boltzmann distribution at the measured temperature. We will focus on Parker's $h_o = 10.5 \text{ MJ/kg}$, $p_o = 54.56 \text{ MPa}$ test case, for which he measured an exit plane velocity of 4517 m/s, temperature in the range of 250 – 300 K, and NO mass fraction of 1.5%. A quick analysis shows that these measurements imply a very small level of internal energy storage in the test-section gas. The total enthalpy of the gas mixture is:

$$h_o = c_p T + e_v + e_{chem} + \frac{1}{2} u^2$$

Here $1/2u^2 = 10.20 \text{ MJ/kg}$, and with $c_p \simeq 1000 \text{ J/kgK}$ and $T = 275 \text{ K}$, we have just 25 kJ/kg remaining in the internal energy modes. With 1.5% NO mass fraction ($h_{NO}^o = 3.0 \text{ MJ/kg}$), the remaining vibrational and chemical energy is essentially zero. Therefore, according to Parker's measurements, the test-section gas has a negligible level of vibrational and chemical energy.

Presumably the differences in the double-cone measurements and simulations are due to problems with the predicted conditions at the exit of the CUBRC LENS-I nozzle. However, MacLean *et al.* (2007) show some improvement in the double-cone results with the use of the CVDV model for vibration-dissociation coupling. In any case, it is important to try to rationalize Parker's results with nozzle flow field models. Therefore, the goal of this work was to reassess the nozzle flow and thermo-chemical modeling approaches to try to improve the prediction of the free-stream conditions.

Recently, Park did a complex, vibrational state-to-state analysis of high-enthalpy nozzle flows [Park (2006)]. His approach solves the vibrational master equation, including state-specific dissociation and recombination processes. The rates are computed with the most accurate approaches available. Park's work is currently the most advanced high-enthalpy nozzle analysis. It showed a number of important things about these flows. First, vibrational non-equilibrium is not an important factor in air. The presence of a large

number of oxygen atoms in the gas causes very rapid relaxation of the vibrational modes. (It is critically important to use the measured data for the $\text{N}_2\text{-O}$ and $\text{O}_2\text{-O}$ relaxation times, rather than the standard Millikan and White relaxation times.) Also, according to Park's analysis there is not a significant over-population of the upper vibrational states. Similarly, the vibrational energy modes of the diatomic species are quite close to one another, with O_2 relaxing slightly more slowly than N_2 . However, from an energy budget perspective, this difference is inconsequential. (Remember that our goal is to track the overall energy budget of these flows – thus full details are not required unless they affect the energy relaxation and redistribution process.) Finally, Park's results for $h_o = 10 \text{ MJ/kg}$, $p_o = 1000 \text{ atm}$ (101.3 MPa) case with similar A/A^* as Parker's LENS-I case gives a nitric oxide mass fraction of 3.92% – significantly higher than measured by Parker. Park's higher reservoir pressure would presumably increase the recombination rates relative to that of Parker, and should therefore be lower than Parker's 1.5%.

3. Nozzle Flow Model

We use a conventional single vibrational energy, thermo-chemical nonequilibrium kinetics model for the nozzle flow. We use 5 chemical species (N_2 , O_2 , NO , N and O) and neglect the effect of ions. The kinetics model is from Park (1988) and we use the same set of vibrational relaxation rate correction factors given by Park to match the available experimental data. We solve the axisymmetric Navier-Stokes equations along with the Spalart-Allmaras turbulence model with a compressibility correction. More details about the nozzle simulation approach are available in Ref. 14. The nozzle code has been used to predict a wide variety of CUBRC reflected shock tunnel nozzle flows [MacLean *et al.* (2005)].

This thermo-chemical model cannot capture vibrational energy inversions, disparate vibrational energy distributions between the diatoms, and the details of vibration-dissociation / recombination interactions. Therefore, we must first validate this approach to show that the model captures the key energy redistribution processes during the expansion of high-enthalpy air. We compare to the 10 MJ/kg, 1000 atm case of Park; we use a conical nozzle of 5 meter length and an exit-to-throat area ratio, A/A^* , of 1000. For this comparison, we treat the flow as inviscid so that the area variation of the nozzle is not affected by the boundary layer displacement. In addition to the full CFD simulation, we compare to a quasi-one-dimensional nozzle calculation. This method includes the complete thermo-chemical model used in the CFD, and simply integrates the governing equations from the throat to the exit plane of the nozzle. Figure 16 compares the CFD and quasi-one-dimensional simulation results for the Park case. Note the excellent agreement between the two methods. Interestingly, the non-uniformities in full CFD simulation cause variations

in the temperature and chemical state, however the final exit conditions are very similar.

The nozzle exit conditions are compared with those of Park in Table 5; note the excellent agreement with the main flow parameters. The present simulations predict slightly lower vibrational temperatures than Park's detailed simulation. Also, we predict a larger NO mass fraction than Park. This is not altogether surprising since there are substantial differences in the model and rates used by Park. Thus, given the large differences in the modeling approach, this agreement is very reasonable. They are also consistent with the comparisons with one- and two-temperature nozzle simulations shown by Park.

Table 5. Computed conditions for Park's 10 MJ/kg nozzle flow case.

	Park	CFD	Quasi-1-D
T (K)	674	684	744
T_v (K)	990	920	936
u (m/s)	4243	4260	4246
ρ (g/m ³)	11.17	11.11	11.02
c_{NO}	3.93	4.86	4.86
c_{O_2}	20.26	20.34	20.65

Table 6. Computed conditions for Parker's 10.5 MJ/kg case (Run 271).

	Parker	CFD
T (K)	250-300	620
T_v (K)		930
u (m/s)	4517	4354
c_{NO}	1.5	5.42
c_{O_2}	20.26	19.10
c_O		1.30

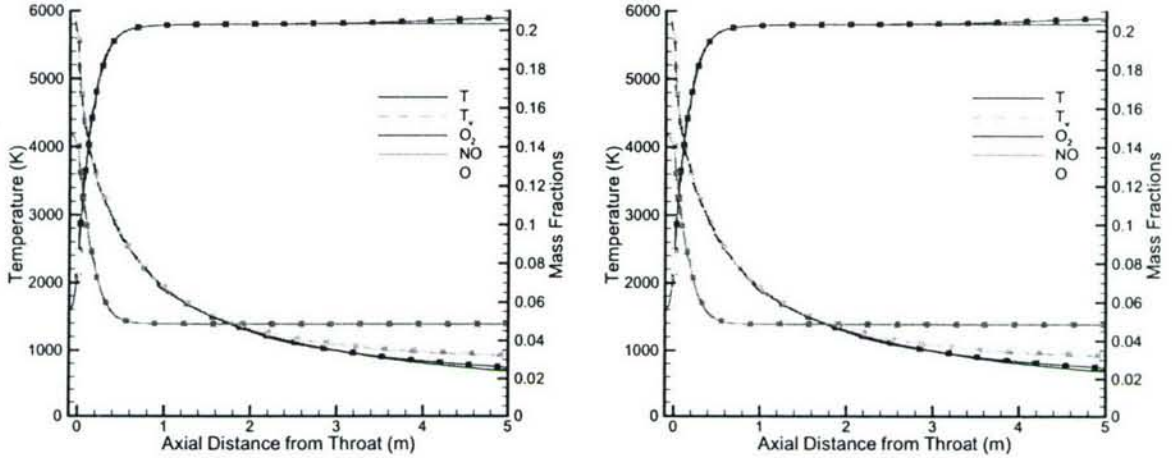


Figure 16. Comparison of full CFD and quasi-one-dimensional simulations of the centerline conditions for Park's 10 MJ/kg test case. Right figure shows an enlargement near the throat.

4. Baseline CUBRC LENS-I Nozzle Simulation

We used the standard thermo-chemical model to simulate the LENS-I nozzle flow at conditions corresponding to the 10.5 MJ/kg and 56.54 MPa run of Parker (Run 271). The resulting nozzle centerline flow field is shown in Figure 17, and the exit plane conditions are compared with the measurements of Parker in Table 6. Note that there is little vibrational nonequilibrium in this case, and that the gas composition freezes near the nozzle throat. We predict an NO mass fraction of 5.42%, significantly above the 1.5% of Parker. Correspondingly, the CFD gives a lower velocity and a higher temperature than measured. Thus, the CFD predicts that a significant amount of energy is stored in the vibrational and chemical energy modes (33 MJ/kg in vibration and 363 kJ/kg chemical energy, compared to approximately 45 MJ/kg in chemical energy for Parker's data).

This is a very significant discrepancy, and is certainly a potential reason for the poor comparison with the double-cone data for high enthalpy air. In the remainder of the section we investigate potential reasons for this difference. It should be noted that our model does not include the full state-to-state kinetics as in Park. However, based on the results of Park and the comparison presented above, it is unlikely that such a model would shed light on this discrepancy. Park did not show any appreciable vibrational population inversion or other effect that could invalidate the present modeling approach. Also, because of the rapid vibrational relaxation in the nozzle, it is unlikely that vibration plays an important role in the chemical kinetics. Rather, we focus on additional issues that are not considered

in conventional nozzle flow models.

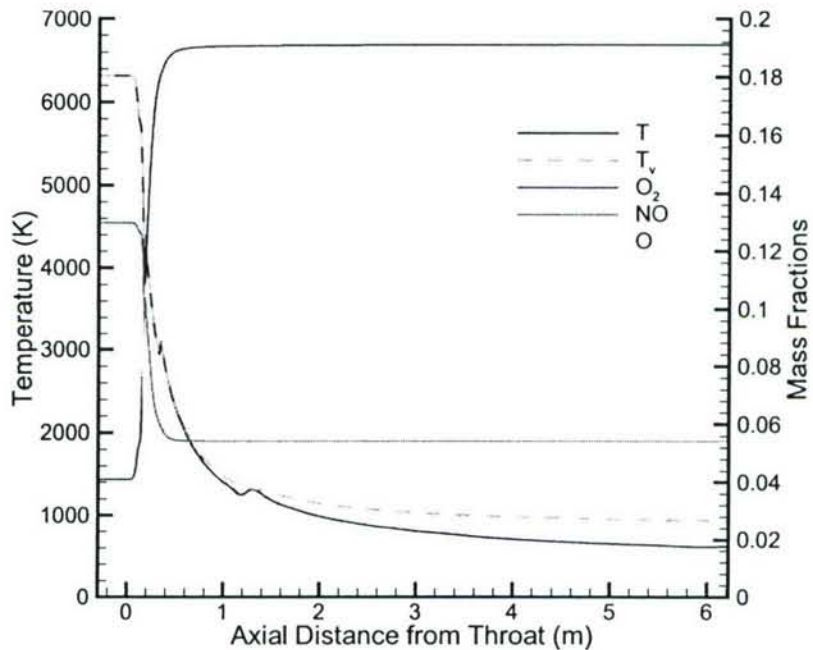
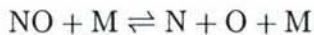


Figure 17. Computed centerline flow conditions for Parker's 10.5 MJ/kg case using the baseline thermo-chemical model.

5. Nitric Oxide Destruction Process

The main issue raised by the comparison with Parker's data is the excessive level of nitric oxide at the nozzle exit plane. Let us consider how NO is consumed as the gas expands from the reservoir (where the NO mass fraction is 13.05%). There are three reactions involving NO. The dissociation/recombination of NO:



and the Zeldovich reactions:



These reactions are written so that they are endothermic as they proceed to the right. During the expansion of the flow in the nozzle, the first reaction proceeds to the left, producing additional NO. The first Zeldovich reaction consumes NO and N atoms (proceeding to the left) in a rapid exothermic reaction. The second Zeldovich reaction also destroys

NO in an endothermic reaction that produces N atoms, which are then used in the first Zeldovich reaction. Therefore, the rate-limiting step is the availability of N atoms. Initially there are N atoms in the reservoir, but these are rapidly consumed by the recombination reaction and the first Zeldovich reaction. Once they are used up, the first reaction cannot take place without N atoms being formed by the second Zeldovich reaction.

Figure 18 illustrates this process more quantitatively by plotting the rate of NO formation as a function of distance for each of the above reactions. We plot the quantity $w_{\text{NO}}/\rho u$, where w_{NO} is the chemical source term for nitric oxide due to each of the three reactions. This gives the non-dimensional rate of NO formation per unit length of the nozzle. In this LENS-I nozzle, the sonic throat is located at approximately 0.154 m from the $x = 0$ location; at this point, the temperature begins to change rapidly, and the gas begins its recombination process. Note that initially the dissociation/recombination reaction produces NO, while the two Zeldovich reactions consume the newly formed NO. Then, as the gas continues to cool the Zeldovich reactions quickly consume the NO, while the recombination reaction produces only a small amount. Note that the two Zeldovich reactions produce NO at essentially the same rate; this confirms that the second reaction is the rate limiting step (especially late in the expansion process). Interestingly, at $x = 0.18$ m there is a sudden reversal of the NO destruction process due to a recompression that increases the centerline temperature. The Zeldovich reactions then continue to consume NO, and by about $x = 0.4$ m the gas has cooled and accelerated so much that the reactions are essentially frozen. Very little reaction occurs in the remainder of the nozzle.

Figure 18 shows that there is a complicated balance between the NO reactions, the rates of formation of the reactants in these reactions. This makes it very difficult to establish which process is critical to the consumption of NO in the nozzle. However, it is clear that the rates of the Zeldovich reactions must play a critical role, as well as the rates of oxygen and nitric oxide dissociation and recombination. Although N atoms play a critical role in the Zeldovich reaction loop, the rate of N atom recombination by three-body processes is so slow that it does not play a role in this flow. Therefore, we consider the sensitivity of the nozzle exit conditions to these critical rates.

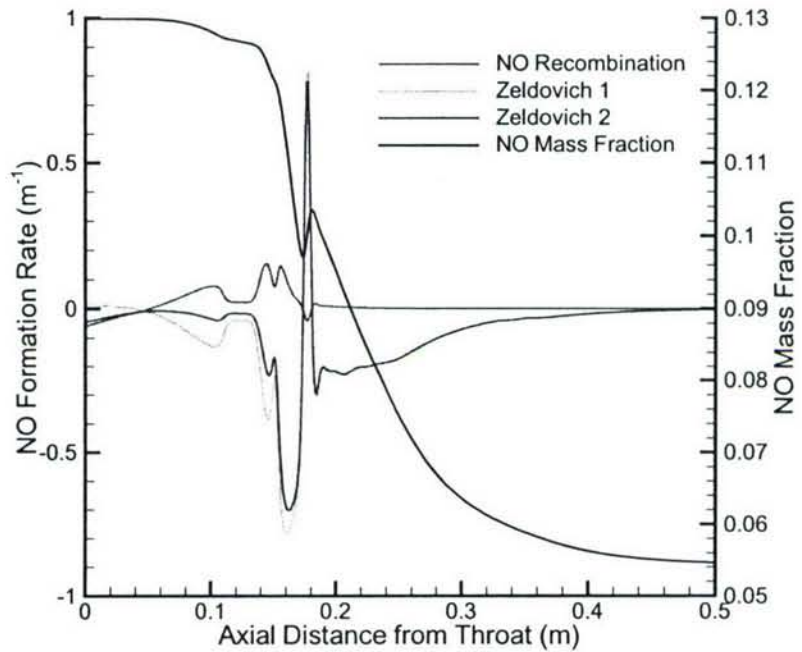


Figure 18. NO formation/destruction rate due to recombination and Zeldovich reactions on nozzle centerline.

Recombination of Oxygen Atoms

A critical process in the nozzle flow is the recombination of oxygen atoms. This takes place through the three-body process of $O + O + M \rightarrow O_2 + M$. At lower temperatures, other processes may play a role in this process (notably O_3). As discussed above, convention dictates that the backward reaction rate is computed from the forward rate via the principle of detailed balance. In equilibrium, this in fact must hold, but there is no reason why the recombination process must be dictated by what is essentially an equilibrium thermodynamic argument. Rather, the recombination process can proceed through many complicated pathways so long as the resulting gas composition reaches an equilibrium condition.

Keck (1960) and Shui *et al.* (1970) develop a variational theory to predict three-body recombination rates; more recently, Korobeinikov (1976) developed a kinetic-theory based approach for computing three-body recombination rates. These theoretical approaches compare favorably with experimental data. Baulch (1973, 1976) compiled the available experimental data for the three-body recombination of O atoms by various collision partners. Figure 19 shows a synthesis of their results for the relevant collision partners. As we

saw from the previous figures, the critical recombination process occurs when the gas is between about 3000 and 6000 K. For this temperature range, there is about a factor of 30 variation in the measured recombination rates; in general the most active collision partner are O atoms, and the least active N₂ molecules. The theoretical rates fall within this general scatter of the experimental data. This huge variation in the data is not surprising given the difficulty of making the rate measurements and the various systems in which they were made.

Also plotted in Figure 19 is the recombination rate based on detailed balance and the dissociation rates used in our work. The strange variation in the rate at temperatures less than 1000 K is because of how the two exponentially varying functions for the forward reaction rate and the equilibrium constant interact with each other at low temperatures. This behavior is not reflected in the data, but it is not important to the nozzle flow since the flow is already frozen by the time it has cooled to 1000 K. In any case, it is clear that our recombination rate with N₂ as collision partners falls well above the experimental data at the critical temperature range. The rate for O-atoms as collision partners is perhaps a little high, but within the general range of the data.

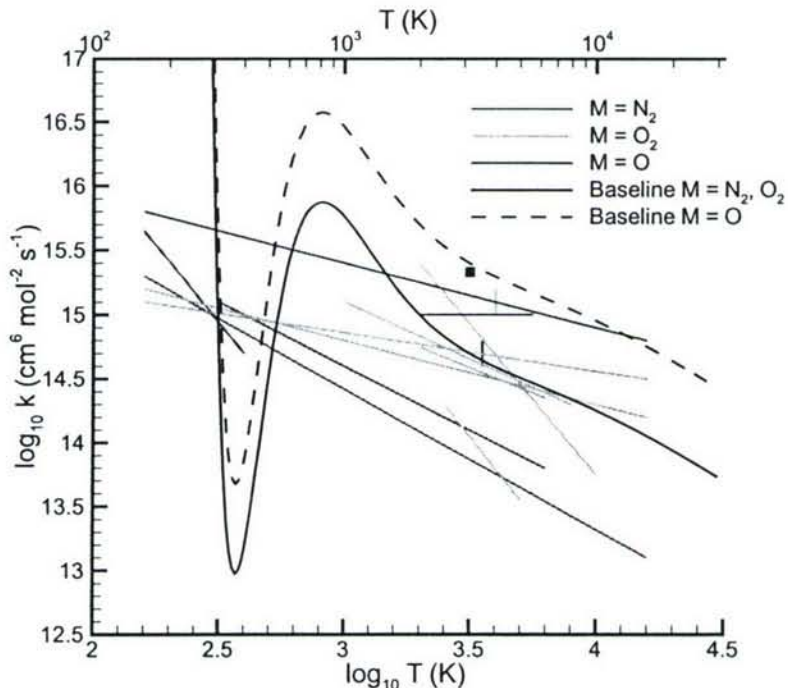


Figure 19. O + O + M recombination rates from Baulch compilation and from detailed balance approach.

Therefore, we could be entitled to reduce the $O + O + N_2 \rightarrow O_2 + N_2$ reaction rate by a significant margin (say by a factor of 10). However, we cannot just lower the rate of this process because then the reservoir gas would no longer be at the proper thermodynamic equilibrium. Thus, we must lower both the forward and backward rate of this reaction to maintain equilibrium in the reservoir. If we make this change to this rate, the resulting nozzle exit plane conditions are a NO mass fraction of 4.46% (down from 5.42%), but a lower velocity of 4317 m/s and a higher O atom mass fraction of 3.10%. Thus, the energy stored in the chemical energy is now 612 kJ/kg, up by a factor of nearly two. Thus, this change moves the nitric oxide level in the right direction, but makes the velocity worse.

Zeldovich Reaction Rates

Given the above discussion of the critical role of the Zeldovich reactions in the recombination of air, it makes sense to consider the effect of these reaction rates. In the present work, we have used the rates of Park: $k_f = 6.4 \times 10^{17} T^{-1} \exp(-38400/T)$ and $k_f = 8.4 \times 10^{12} \exp(-19450/T)$ (cm³/moles) for the first and second Zeldovich reactions. However, there is a very large scatter in the measured rates. (We will spare the reader additional plots showing this variation; these are readily available in the Baulch *et al.* publications.) Also, quasi-classical trajectory calculations show that the Park rates are questionable at higher temperatures [Bose *et al.* (1996, 1997) These calculations using accurate potential energy surfaces should increase in accuracy at high temperature, contrary to the experimental data. Therefore, let us consider the effect of using these QCT rates in the nozzle flow field.

We have run several cases with the Bose QCT rates; in all cases, the nitric oxide mass fraction increases at the nozzle exit plane. Using these rates for both reactions gives a NO mass fraction of 6.70%; this is primarily due to the slower forward rate of the first Zeldovich reaction. Thus, the nozzle flow is sensitive to these rates, it does not appear that accepted rate expressions result in improved agreement with the Parker data.

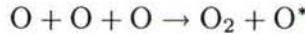
Possible Role of Excited Electronic States

The reservoir temperature (6318 K) is sufficiently high that they could play a role in the recombination process. The important electronic states are the 1D_2 state of O-atoms (2.0 eV above ground) and the $a^1\Delta_g$ and $b^1\Sigma_g^+$ states of O₂ molecules (1.0 and 1.6 eV above ground). All of these states are metastables, with long radiative lifetimes. There are various ways in which these species could play a role in the recombination process. However, accepted chemical kinetics mechanisms and associated rates are not available. Therefore, we must postulate possible processes and assume reasonable rates to provide a rough bounds for their relevance.

First consider first excited state of O atoms; denoting this state as O*, it is possible that the second Zeldovich reaction could be accelerated by this species. The reaction



is now exothermic because of the elevated heat of formation of O*. Presumably, this reaction would be very fast, resulting in the rapid destruction of NO and the formation of N atoms that can participate in the first Zeldovich reaction. However, there is a limited supply of O* unless there is a means of generating it during the expansion. The only obvious process is



which would yield an O* atom due to the exothermic recombination of O₂ by O atom interactions. This reaction has the potential to produce a significant number of electronically excited species.

We implemented these reactions in the quasi-one-dimensional code and reran Park's case. To do so, we must assume several rate constants, and assess the sensitivity of the results to the choice of the unknown rate constants. Previously, we saw that the recombination rate of O₂ via ground state species is highly uncertain; clearly the rates that we need for these reactions are even more uncertain. Thus, the purpose here is to see if this process has any potential importance in the nozzle flow. Here we take the most favorable assumption that the O* species do not radiatively or collisionally decay; rather they are only destroyed via the above reactions. Also, to provide an upper bound, we assume that all O + O + O reactions result in the formation of O*.

In order to implement the above model, we need an expression for the equilibrium constants for the reactions. We use statistical mechanics to get:

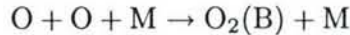
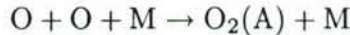
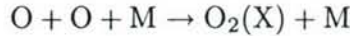
$$\frac{[\text{O}^*]}{[\text{O}]} = \frac{g_1 e^{-\theta_1/T}}{g_0 + g_1 e^{-\theta_1/T}}$$

with $g_0 = 9$, $g_1 = 5$, and $\theta_1 = 22830 \text{ K}$. This expression can then be used to adjust the ground-state equilibrium constants for the reactions involving O*.

We find that this mechanism does not appear to play an important role in NO destruction. There is only a small number (0.18% mass fraction) of O* atoms in the reservoir. Their number diminishes quickly as the gas expands due to the very strong dependence of the equilibrium excited state fraction on temperature. Furthermore, the O₂ recombination process does not form many excited state species, again because of the extreme temperature dependence on the equilibrium constant for this reaction. This conclusion appears to be independent of the assumed rates for these reactions.

There is at least one caveat to the conclusion that the O excited state does not play a role in the destruction of NO. We have assumed a simple kinetics model for O*, however if there were additional reaction pathways, it may be possible to sustain a larger level of excited atoms within the nozzle. However, this will require much more work.

Now let us turn to the role of the electronically excited states of O₂. During the recombination of oxygen, the following reactions could occur:



That is, the oxygen molecules could recombine to electronically excited states. These species would store additional chemical energy, and would presumably be highly reactive. Again, we face the issue that there are no available rate data for these reactions. However, Keck uses his variational theory approach to predict these rates; he shows that the recombination to the A state is about a factor of two slower than to the ground state, and recombination to the B state is about a factor of ten slower. Thus, there does not appear to be any favoring of these reactions. Furthermore, these reactions would store additional chemical energy and would further delay the relaxation process. As such, it appears that if anything, the excited O₂ states would tend to make the agreement with Parker's data even worse.

Additional Comments

Without resorting to random and aphysical modifications of the chemical kinetics model, we cannot obtain the low levels of NO measured by Parker in the LENS-I nozzle. There could be additional processes that we have not considered. Again, it should be stressed that these effects must be quite large.

For example, there is N₂O and NO₂ in the reservoir (at levels of about 0.03% to 0.04%). A simple kinetics model shows that these species are rapidly destroyed during the expansion, and do not play a role in the destruction of NO. We have neglected the presence of ions in our analysis; NO⁺ is the most prevalent ion at 8.1×10^{-5} mass fraction. There are additional trace species that could potentially play a role, though again these are present at only low levels.

6. Conclusions

In this report we consider the flow of high-enthalpy air in the CUBRC LENS-I nozzle. We compare with recent non-intrusive laser absorption measurements of Parker *et al.* (2006, 2007) in an attempt to better understand this flow. Parker's measurements show a high velocity, very little internal energy excitation, and a low (1.5% by mass) level of nitric oxide at the nozzle exit plane. Our calculations predict a significantly higher level of NO (5.42%), in reasonable agreement with more detailed simulations of Park (2006). We also predict a correspondingly low velocity and a higher level of internal energy excitation than Parker. We investigate possible reasons for this large discrepancy. We vary the Zeldovich rates within reasonable bounds from the literature, and we use experimental data to modify the O₂ recombination rate. We also consider the possible role of electronically excited O₂ and O, as well as other trace species. These changes make some differences to the predicted NO mass fraction, but they are relatively minor. At this point, we cannot reproduce Parker's measurements using kinetics models that are within the bounds of reality.

VI. Summary

During the past three years, we have worked to develop and analyze a high-enthalpy flow dataset for CFD code validation. In collaboration with CUBRC Inc. personnel, we designed the experimental conditions for the double-cone geometry used in previous low-enthalpy nitrogen tests. We then used our standard CFD codes and thermo-chemical models to analyze these flows. In general, the comparisons with nitrogen flows are good, even at high enthalpy (10 MJ/kg). But the comparisons between predictions and experiments for air above 5 MJ/kg is poor. We find that as the enthalpy increases, the agreement gets worse. In particular, the CFD predicts that the separation zone decreases in size much more rapidly than given in the experiments.

We have attempted to understand the source of this discrepancy. Based on our previous work with nitrogen, we were concerned that the nozzle flow field was not predicted correctly. We therefore spent a lot of time assessing the sensitivity of the nozzle test section conditions to the thermo-chemical model used to predict the nozzle flow field. We used a vibrational state-specific model to assess the possibility of non-Boltzmann vibrational energy distributions in the nozzle – this was completely unsuccessful in explaining the observed discrepancies. We then made a careful study of the assumptions implicit in the thermo-chemical model for air. Again, these efforts were also in vain. Therefore, we must conclude that there is another unknown explanation for the discrepancy between the measurements and the simulations. Future work will involve a study of how the reservoir flow behaves during the shock reflection from the end-wall of the shock tunnel. We postulate that the reservoir flow does not reach equilibrium before expanding through the nozzle; clearly this would change the facility test-section conditions.

Acknowledgments

This work was sponsored by the Air Force Office of Scientific Research under grant FA9550-04-1-0114. The views and conclusions contained herein are those of the author and should not be interpreted as necessarily representing the official policies or endorsements, either expressed or implied, of the AFOSR or the U.S. Government.

References

Adamovich, I., Macheret, S.O., Rich, J.W. and Treanor, C.E., (1998) "Vibrational Energy Transfer Rates Using a Forced Harmonic Oscillator Model," *Journal of Thermophysics and Heat Transfer*, **12** (1), pp. 57-65.

Adamovich, I. and Rich, J.W., (1998) "Three-Dimensional Nonperturbative Analytic Model of Vibrational Energy Transfer in Atom-Molecule Collisions," *Journal of Chemical Physics*, **109** (18), pp. 7711-7724.

Anderson, J. D., (1989) *Hypersonic and High Temperature Gas Dynamics*, McGraw-Hill.

Baldwin, B. S. and Lomax, H., (1978) "Thin Layer Approximation and Algebraic Model for Separated Turbulent Flows," *AIAA Paper No. 78-257*.

Baulch, D.L., D.D. Drysdale, D.G. Horne, and A.C. Llyod, (1973) *Evaluated Kinetic Data for High Temperature Reactions*, Vol. 2, Butterworths.

Baulch, D.L., D.D. Drysdale, J. Duxbury, and S. Grant, (1976) *Evaluated Kinetic Data for High Temperature Reactions*, Vol. 3, Butterworths.

Birch, S. F. and Keyes, J. W., (1972) "Transition in Compressible Free Shear Layers," *Journal of Spacecraft and Rockets*, **9** (8), pp. 623-624.

Black, G., Wise, H., Schechter, S., and Sharpless, R. L., (1974) "Measurements of vibrationally excited molecules by Raman Scattering. II. Surface Deactivation of vibrationally excited N₂," *J. Chem. Phys.*, **60** (9), pp. 3526-3536.

Blottner, F. G., Johnson, M., and Ellis, M., (1971) "Chemically Reacting Viscous Flow Program for Multi-Component Gas Mixtures," Sandia Laboratories Report No. SC-RR-70-754, Albuquerque, New Mexico.

Bose, D. and G.V. Candler, (1996) "Thermal Rate Constants of the N₂ + O → NO + N Reaction Using ab initio ³A'' and ³A' Potential Energy Surfaces," *Journal of Chemical Physics*, Vol. 104, No. 8, pp. 2825-2833.

Bose, D. and Candler, G.V., (1997) "Thermal Rate Constants of the O₂ + N → NO + O Reaction Based on the ²A' and ⁴A'' Potential Energy Surfaces," *Journal of Chemical Physics*, **107** (16), pp. 6136-6145.

Boyd, I. D., Chen, G., and Candler, G. V., (1995) "Predicting Failure of the Continuum Fluid Equations in Transitional Hypersonic Flows," *Phys. of Fluids*, **7** (1), pp. 210-219.

Bray, K.N.C., (1968) "Vibrational Relaxation of Anharmonic Oscillator Molecules: Relaxation Under Isothermal Conditions," *Journal of Physics B, Proceedings of the Physical Society*, Vol. 1, Ser. 2, pp. 705-717.

Bray, K.N.C., (1970) "Vibrational Relaxation of Anharmonic Oscillator Molecules II: Relaxation Under Non-Isothermal Conditions," *Journal of Physics B, Atomic and Molecular Physics*, **3** (11), pp. 1515-1538.

Candler, G. V., (1988) "The Computation of Weakly Ionized Hypersonic Flows in Thermochemical Nonequilibrium," *Ph.D. Thesis*, Stanford University.

Candler, G. V., Nompelis, I., and Holden, M. S., (2000) "Computational Analysis of Hypersonic Laminar Viscous-Inviscid Interactions," *AIAA Paper No. 2000-0532*.

Candler, G. V., Nompelis, I., and Druguet, M.-C., (2001) "Navier-Stokes Predictions of Hypersonic Double-Cone and Cylinder-Flare Flow Fields," *AIAA Paper No. 2000-1024*.

Candler, G. V., Nompelis, I., Druguet, M.-C., Holden, M. S., Boyd, I. D., and Wang, W.-L., (2002) "CFD Validation for Hypersonic Flight: Hypersonic Double-Cone Flow Simulations," *AIAA Paper No. 2002-0581*.

Candler, G. V. and Nompelis, I., (2002) "CFD Validation for Hypersonic Flight: Real Gas Effects," *AIAA Paper No. 2002-0434*.

Catris, S. and Aupoix, B., (2000) "Density Corrections for Turbulence Models," *Aerospace Sci. Technol.*, **4**, pp. 1-11.

Center, R. E., and Caledonia, G. E., (1972) "Anharmonic Effects on the Rate of Relaxation of Vibrational Energy in Rapidly Expanding Flows," *Journal of Chemical Physics*, Vol. 57, No. 9, pp. 3763-3770.

Druguet, M.-C., Candler, G. V., and Nompelis, I., (2002) "Navier-Stokes Computations of Hypersonic Double-Cone Flows: Influence of Numerics," Proceedings of the West East High Speed Flow Field Conference, Marseille, France.

Druguet, M.-C., Candler, G. V., and Nompelis, I., (2003) "Simulations of Viscous Hypersonic Double-Cone Flows: Influence of Numerics," *AIAA Paper No. 2003-3548*.

Gaitonde, D., Canupp, P. W., and Holden, M. S., (2002) "Heat Transfer Predictions in a Laminar Hypersonic Viscous/Inviscid Interaction," *Journal of Thermophysics and Heat Transfer*, **16** (4), pp. 481-489.

Gnoffo, P. A., (2001) "CFD Validation Studies for Hypersonic Flow Prediction," *AIAA Paper No. 2001-1025*.

Gökçen, T., (1989) "Computation of Hypersonic Low Density Flows with Thermochemical Nonequilibrium," *Ph.D. Thesis*, Stanford University.

Harvey, J. K., Holden, M. S., and Wadhams, T. P., (2001) "Code Validation Study of Laminar Shock/Boundary Layer and Shock/Shock Interactions in Hypersonic Flows. Part

B: Comparison with Navier-Stokes and DSMC Solutions," *AIAA Paper No. 2001-1031*.

Hirsch, C. (1991) *Numerical Computation of Internal and External Flows*, Wiley, New York.

Holden, M. S. (1998) "Shock Interaction Phenomena in Hypersonic Flows," *AIAA Paper No. 98-2751*.

Holden, M. S. (2000) "Experimental Studies of Laminar Separated Flows Induced by Shock Wave/Boundary Layer and Shock/Shock Interaction in Hypersonic Flows for CFD Validation," *AIAA Paper No. 2000-0930*.

Holden, M. S. and Wadhams, T. P., (2001) "Code Validation Study of Laminar Shock/Boundary Layer and Shock/Shock Interactions in Hypersonic Flows. Part A: Experimental Measurements," *AIAA Paper No. 2001-1031*.

Holden, M. S. (2004) "Experimental Studies in LENS Shock and Expansion Tunnel to Examine Real-Gas Effects in Hypervelocity Flows," *AIAA Paper No. 2004-0916*.

Josyula, E., and Bailey, W. F., (2004) "Vibrational Population Enhancement in Nonequilibrium Dissociating Hypersonic Nozzle Flows," *Journal of Thermophysics and Heat Transfer*, **18** (4), pp. 550-553.

Keck, J.C., (196) "Variational Theory of Chemical Reaction Rates Applied to Three-Body Recombinations," *Journal of Chemical Physics*, Vol. 32, No. 4, pp. 1035-1050.

Korobeinikov, Y.G., (1976) "Calculation of Three-Body Recombination Rate Constants," *Combustion, Explosion and Shock Waves*, Vol. 11, No. 6, pp. 737-743.

Laney, C. B. (1998) *Computational Gasdynamics*, Cambridge Univ. Press.

Lee, J.-H. (1985) "Basic Governing Equations for the Flight Regimes of Aeroassisted Orbital Transfer Vehicles," *Thermal Design of Aeroassisted Orbital Transfer Vehicles*, H. F. Nelson (Ed.), Progress in Aeronautics and Astronautics, **96**, pp. 3-53.

Lukasiewicz, J., (1973) *Experimental Methods of Hypersonics*, Gasdynamics Series, **3**, Marcel Dekker.

MacLean, M., Candler, G. V. and Holden, M. S., (2005) "Numerical Evaluation of Flow Conditions in the LENS Reflected Shock-Tunnel Facilities," *AIAA Paper No. 2005-0903*.

MacLean, M., M. Holden, T. Wadhams and R. Parker, (2007) "A Computational Analysis of Thermochemical Studies in the LENS Facilities," *AIAA-2007-0121*.

Meolans, J. G. and Graur, I. A., (2002) "Thermal Slip Boundary Conditions at the Wall in Nonequilibrium Flows," *Proceedings of the West East High Speed Flow Fields 2002*

Conference, Marseilles, France, Apr. 2002.

Millikan, R. C. and White, D. R., (1953) "Systematics of Vibrational Relaxation," *J. Chem. Phys.*, **39**, pp. 3209-3213.

Nompelis, I., Candler, G. V., Holden, M. S. and Wadhams, T. P., (2003) "Real Gas Effects on Hypersonic Shock Wave Laminar Boundary Layer Interactions," *AIAA Paper No. 2003-0443*.

Nompelis, I., Candler, G. V., Holden, M. S. and Wadhams, T. S., (2003) "Computational Investigation of Hypersonic Viscous/Inviscid Interactions in High Enthalpy Flows," *AIAA Paper No. 2003-3642*.

Nompelis, I., Candler, G. V. and Holden, M. S., (2003) "Effect of Vibrational Nonequilibrium on Hypersonic Double-Cone Experiments," *AIAA Journal*, **41** (11), pp. 2162-2169.

Nompelis, I., Candler, G. V., Wadhams, T. P. and Holden, M. S., (2003) "Numerical Simulation of High-Enthalpy Experiments in the LENS-X Expansion Tube Facility," *AIAA Paper No. 2004-1000*.

Nompelis, I., (2004) "Computational Study of Hypersonic Double-Cone Experiments for Code Validation," *Ph.D. Thesis*, University of Minnesota.

Nompelis, I., G.V. Candler, M. MacLean, T.P. Wadhams, and M.S. Holden, (2005) "Numerical Investigation of High Enthalpy Chemistry on Hypersonic Double-Cone Experiments," *AIAA Paper No. 2005-0584*.

Olejniczak, J., Wright, M. J. and Candler, G. V., (1997) "Numerical Study of Inviscid Shock Interactions on Double-Wedge Geometries," *J. Fluid Mech.*, **352**, pp. 1-25.

Olejniczak, J., Candler, G. V., and Hormung, H. G., (1997) "Computation of Double-Cone Experiments in High Enthalpy Nitrogen," *AIAA Paper No. 97-2549*.

Olejniczak, J., (1997) "Computational and Experimental Study of Nonequilibrium Chemistry in Hypersonic Flows," *Ph.D. Thesis*, University of Minnesota.

Olejniczak, J., Candler, G. V., Wright, M. J., Leyva, I. and Hormung, H. G., (1999) "An Experimental and Computational Study of High Enthalpy Double-Wedge Flows," *Journal of Thermophysics and Heat Transfer*, **13** (4), pp. 431-440.

Park, C., (1985) "On Convergence of Computation of Chemically Reacting Flows," *AIAA Paper No. 85-0247*.

Park, C., (1986) "Assessment of Two-Temperature Kinetic Model for Dissociating and Weakly Ionizing Nitrogen," *AIAA Paper No. 86-1347*.

Park, C., (1988) "Two Temperature Interpretation of Dissociation Rate Data for N₂ and O₂," *AIAA Paper No. 88-0458*.

Park, C., (1990) *Nonequilibrium Hypersonic Aerothermodynamics*, John Wiley & Sons.

Park, C., (1990) "Thermochemical Relaxation in Shock Tunnels," *Journal of Thermophysics and Heat Transfer*, **90** (4), pp. 689-698.

Park, C., (2006) "Thermochemical Relaxation in Shock Tunnels," *Journal of Thermophysics and Heat Transfer*, Vol. 20, No. 4, pp. 689-698.

Parker, R., Wakeman, T., Holden, M. S., and MacLean, M., (2006) "Measuring Nitric Oxide Freestream Concentration Using Quantum Cascade Lasers at CUBRC," *AIAA Paper No. 2006-0926*.

Parker, R., and Wakeman, T., (2007) "Measuring Nitric Oxide Freestream Velocity Using Quantum Cascade Lasers at CUBRC," *AIAA Paper No. 2007-4329*.

Ruffin, S.M., (1995) "Prediction of Vibrational Relaxation in Hypersonic Expanding Flows Part 1: Model Development," *Journal of Thermophysics and Heat Transfer*, **9** (3), pp. 432-437.

Ruffin, S.M., (1995) "Prediction of Vibrational Relaxation in Hypersonic Expanding Flows Part 2: Results," *Journal of Thermophysics and Heat Transfer*, **9** (3), pp. 438-445.

Roy, C. J., Gallis, M. A., Bartel, T. J., and Payne, J. L., (2001) "Navier-Stokes and Direct Simulation Monte Carlo Predictions for Laminar Hypersonic Separation," *AIAA Paper No. 2001-1024*.

Sandrers, R., Morano, E. and Druguet, M.-C., (1998) "Multidimensional Dissipation for Upwind Schemes Stability and Applications to Gas Dynamics," *J. of Computational Physics*, **145** (2), pp. 511-537.

Schaaf, S.A. and Chambre, P. L., (1966) *Flow of Rarefied Gases*, Princeton Univ. Press.

Shui, V.H., J.P. Appleton, J.C. Keck, (1970) "Three-Body Recombination and Dissociation of Nitrogen: A Comparison between Theory and Experiment," *Journal of Chemical Physics*, Vol. 53, No. 7, pp. 2547-2558.

Spalart, P. R. and Allmaras, S. R., (1992) "A One-Equation Turbulence Model for Aerothermodynamic Flows," *AIAA Paper No. 92-0439*.

Steger, J. L. and Warming, R. F., (1981) "Flux Vector Splitting for the Inviscid Gasdynamic Equations with Application to Finite Difference Methods," *J. Comp. Phys.*, **40**, pp. 263-293.

Toro, E. F., (1997) *Riemann Solvers and Numerical Methods for Fluid Dynamics*, Springer.

Treanor, C.E., Rich, J.W. and Rehm, R.G., (1968) "Vibrational Relaxation of Anharmonic Oscillators with Exchange-Dominated Collisions," *Journal of Chemical Physics*, Vol. 48, No. 4, pp. 1798-1807.

Vincenti, W. G. and Kruger, C. H., (1982) *Introduction to Physical Gas Dynamics*, Krieger Publishing Company.

Wadhams, T. P. and Holden, M. S., (2003) "Experimental Studies and Numerical Predictions for Hypervelocity Vehicle Design and Code Validation," AIAA Paper No. 2003-6905.

Wilke, C. R., (1950) "A Viscosity Equation for Gas Mixtures," *J. Chem. Phys.*, **18**, pp. 517-519.

Wright, M. J., (1997) "A Family of Data-Parallel Relaxation Methods for the Navier-Stokes Equations," *Ph.D. Thesis*, University of Minnesota.

Wright, M. J., Bose, D., and Candler, G. V., (1998) "A Data-Parallel Line Relaxation Method for the Navier-Stokes Equations." *AIAA Journal*, **36** (9), pp. 1603-1609.

Wright, M. J., Sinha, K., and Candler, G. V., (1999) "The Effect of Turbulence on Double-Cone Shock Interactions," *AIAA Paper No. 99-0146*, Jan. 1999.

Wright, M. J., Sinha, K., Olejniczak, J., Candler, G. V., Magruder, T. D. and Smits, A. J., (2000) "Numerical and Experimental Investigation of Double-Cone Shock Interactions," *AIAA Journal*, **38**(12), pp. 2268-2276.